國立臺灣大學理學院地質科學系

碩士論文

Department of Geosciences

College of Science

National Taiwan University

Master Thesis

重建末次冰期以來南海西部表層海水酸鹼值及水文特性

Deglacial changes in surface ocean pH and hydrologic condition in the western South China Sea

孫韻如

Yun-Ju Sun

指導教授：黃國芳 博士

任昊佳 博士

Advisor: Kuo-Fang Huang, Ph.D.

Hao-Jia Ren, Ph.D.

中華民國 106 年 8 月

August 2017

國立臺灣大學碩士學位論文
口試委員會審定書

重建末次冰期以來南海西部表層海水酸鹼值及水文特性
Deglacial changes in surface ocean pH and hydrologic condition in the western South China Sea

　　本論文係孫韻如君（學號 R03224207）在國立臺灣大學地質科學系、所完成之碩士學位論文，於民國 106 年 7 月 3 日承下列考試委員審查通過及口試及格，特此證明

口試委員：

_____

（指導教授）

黃國芳

_____

（指導教授）

鍾令和

_____

致謝

　　本論文的完成要特別感謝這一年半以來，在地化領域中遇到的每位師長及學長姐們，由衷的感謝大家的指導及陪伴，開啟一個我從未想像過的視界。尤其特別感謝指導教授黃國芳老師，謝謝學長的提攜，願意指導一個完全新手學習古海洋、地球化學及儀器分析的專業知識以及手把手的實驗操作，同時也期許自己能在學習上同學長般嚴謹，並且敦厚待人；同時也感謝台大共同指導教授任昊佳老師，在邏輯縝密的古氣候學的框架之下對於本論文的諸多提點；感謝口試委員鍾全雄博士在實驗設計上的寶貴建議，並謝謝魏國彥老師在口試時提出的討論及反饋；感謝劉志飛老師提供珍貴的有孔蟲樣本及岩心資料，也感謝洪崇勝老師對於此研究領域的大力支持，並提供樣本處理上的協助。在此感謝各位師長的建議及指正，提供這樣難得的經驗並使研究工作更臻完善。另外感謝大學專題的指導教授楊耿明老師，謝謝老師從大三以來的指導及經驗分享，除了認識在震測解釋背後所需要的理論基礎外更多是對台灣地質的熱情，以及海研專題的劉家瑄老師，老師對於海洋科學的熱愛也啟發了我，很開心過去能有機會在船上向您學習。感謝鄧屬予老師對於研究亮點的提點仍銘記在心。

　　感謝這些日子遇到的大家：特別謝謝若梅學姐及明宗學長帶我從零開始做實驗及操作儀器，真的非常感謝兩位耐心和細心的指導；謝謝實驗室的佩穎學姐、敏如學姐、許大哥、柏兆學長、沛壕學長、永欣學姐（和可愛的橙橙）在每次的討論和實驗當中獲益良多，有你們相伴一起經歷碩班的大小事；謝謝國航學長及俊宏學長在有孔蟲的辨識及挑蟲上的各種協助；謝謝智凱學長在課程和口試上的討論及鼓勵；謝謝中研院601室的資詠、易璇以及妮容、景雲在各種事務上的協助及解答，下午的點心時光總特別歡樂。謝謝在最後關頭奮力一起努力的雅蘘和晏欣，互相支持度過難關；謝謝一起北上的成大同窗，也感謝這漫漫三年當中好友們的鼓勵才得以支撐下去。

　　最後感謝這一路走來總是支持我的家人們。真心感謝林冠這六年來的陪伴，尤其是在這些過程中，能與你一同成長的我非常幸運；謝謝爸媽和妹妹們的支持，我才得以順利的完成學業，誠心祈求父親能早日康復也感謝母親的辛勞。謝謝！

摘要

解構古海洋碳循環及重建水文特徵有助於瞭解未來氣候在冰期/間冰期尺度下的變化。在末次冰消期間，深海儲存的二氧化碳隨著大洋湧升流上湧至表水，成為現今大氣中的二氧化碳的主要來源。現今的海洋學研究已知，由於大尺度海陸交互作用的影響，邊緣海對於驟變氣候的反應較大洋靈敏。然而，目前研究對於此時間段下邊緣海所扮演之角色仍瞭解甚少。因此，本研究試圖重建南海西部在末次冰消期間的表層海水酸鹼值及水文狀態（表層海水溫度、湧升強度）。本研究首先建立一套可量測少量有孔蟲殼體的硼同位素及微量元素比值的方法，利用微昇華技術純化硼同位素，並搭配多接收器感應耦合電漿質譜儀(MC-ICP-MS)及高解析感應耦合電漿質譜儀(HR-ICP-MS)，對於硼同位素的分析精準度可優於 0.30‰ (2SD)，而微量元素比值（Mg/Ca, B/Ca, Li/Ca, Ba/Ca and U/Ca）可優於 2.0 % (2SD)。

本研究分析取自岩心 MD05-2901 中的浮游有孔蟲 (*Globigerinoides sacculifer*) 並應用多個代用指標來研究末次冰期以來南海西部表層海洋的海水酸鹼值及水文特性。研究結果顯示，南海西部在末次冰消期間釋放出相較於現今更多的二氧化碳，成為大氣中二氧化碳的來源 (source)。在此時間段下，整個南海海水表溫主要受到緯度的影響，並且冰期時西部南海的海水表溫與晚全新世的海溫約相差 3 度。此外，結合有孔蟲殼體 Ba/Ca 所重建的湧升強度可得知，南海西部的水文特徵主要受東亞夏季季風所控制。

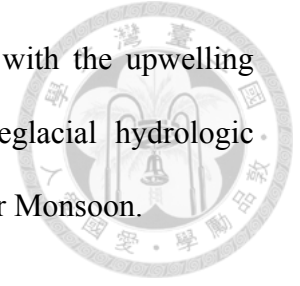關鍵詞：**南海、硼同位素、pH 值代用指標、微量元素比值代用指標**

Abstract

Deciphering ocean carbon system and hydrologic variability is a key to further our understanding of global carbon cycle and climate dynamics within the glacial-interglacial cycles. During the last deglaciation, oceanic carbon dioxide (CO_2) outgassed from upwelling regions in the open ocean has been considered to be the main source of CO_2 in the atmosphere. However, marginal seas receive less attention despite they are potential CO_2 sources based on the modern observations and more sensitive to abrupt climate changes through ocean-atmosphere teleconnection. In this study, we focus on reconstructing surface ocean pH and hydrologic conditions (sea surface temperature and upwelling intensity) in the western South China Sea (W-SCS) during the last deglaciation.

A new analytical protocol is established for measuring the isotopic composition of boron ($\delta^{11}B$) and trace element ratios (TEs) in small sample sizes (< 2 mg) of foraminifera using MC-ICP-MS and HR-ICP-MS, respectively. By applying micro-sublimation technique, the external precision for $\delta^{11}B$ determination is better than ± 0.30 ‰ (2SD), while for TEs (e.g. Mg/Ca, B/Ca, Li/Ca, Ba/Ca and U/Ca) is better than ± 2.0 %, (2SD). Multi-proxies approach is applied for planktonic foraminifera (*Globigerinoides sacculifer*, mixed-layer dwelling species) collected from sediment core MD05-2901 (water depth 1454 m, located at the summer upwelling region off middle Vietnam) in the W-SCS

The reconstructed surface water pH values derived from the $\delta^{11}B$ values suggest that the W-SCS was a CO_2 source throughout the last deglaciation, and the flux of CO_2 was greater than that of the modern condition. This is most likely influenced by the degree of the basin-wide vertical mixing within the entire SCS basin during the last deglaciation. The Mg/Ca-SST record indicates a latitudinal control since the Last Glacial Maximum, and the late

iii

Holocene SST was ~3°C higher than the glacial period. Combining with the upwelling intensity derived from the foraminifera-based Ba/Ca record, the deglacial hydrologic variability in the W-SCS is mainly controlled by the East Asian Summer Monsoon.

Keywords: South China Sea, Boron isotopes pH-proxy, Trace element ratios multi-proxies

Content

Figure Content

Table Content

CHAPTER 1   INTRODUCTION

1.1 Impact of atmospheric CO_2 on climate change and its behavior in marginal seas

Recently, the rapid increase of carbon dioxide (CO_2) in the atmosphere has become the main focus for climate issues since the anticipated warming and associated environmental changes truly affect the human civilization and global terrestrial–marine ecosystems. As the largest CO_2 reservoir, ocean plays a critical role of global climate system (Hönisch et al., 2012, Fig 1.1). Throughout the air-sea interaction, the CO_2 concentration in the atmosphere is determined by a balance with the surface areas of the ocean that are supersaturated or undersaturated with respect to the atmospheric CO_2 content (Fig 1.2). In order to improve our current understanding of global carbon cycle, reconstructing changes in atmospheric CO_2 and seawater pH in the geological past should be a feasible approach (Foster and Rae, 2016 and references therein). Additionally, studying the driving mechanism and natural fluctuations of paleoclimate will provide a better constraint on the prediction of the future atmospheric CO_2 variation and the response of the Earth's system to changing climate.

For the geological time scale, Earth surface temperature co-varied with atmospheric CO_2 suggests that CO_2 may be an important driving force for Earth's climate in the glacial-interglacial cycles (Cuffey and Vimeux, 2001). During the last deglaciation, an isolated glacial deep ocean carbon reservoir released CO_2 to the atmosphere through upwelling region at Southern Ocean and East Pacific Ocean, driving the atmospheric CO_2 to rise and leads to high CO_2 concentration during the Holocene (Martínez-Botí et al., 2015). This highlights the role of the ocean in global carbon cycle and the distributions of CO_2 in the ocean and atmosphere, along with the important influences of these interactions on geological events.
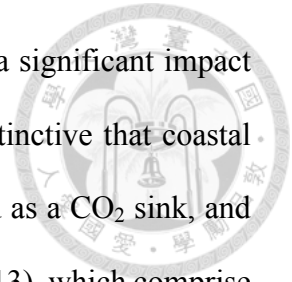
On the other hand, the coastal ocean is recently observed to have a significant impact on the global carbon budget (e.g. Cai, 2011; Cai et al., 2006). It is instinctive that coastal oceans are abundant in nutrients and high in productivity, thus regarded as a CO_2 sink, and the global coastal ocean sea-air CO_2 flux is -0.36 Pg C yr^{-1} (Dai et al., 2013), which comprise 21% global ocean net CO_2 flux of -1.4 Pg C yr^{-1} (Takahashi et al., 2009). As a dynamic component for the global carbon cycle, coastal ocean could act as either the atmospheric CO_2 sink or source in different areas. The latter one is more of scientific interest. The Ocean-dominated Margin (OceMar) systems are provided as a hypothesis to explain CO_2 degassing which the main controlling factor is characterized by dynamic interaction with the open ocean rather than local sources (Dai et al., 2013). Though modern observation highlighted the important of coastal oceans in global carbon budget, however, the behavior of CO_2 in marginal seas throughout the geological history remains largely unknown.
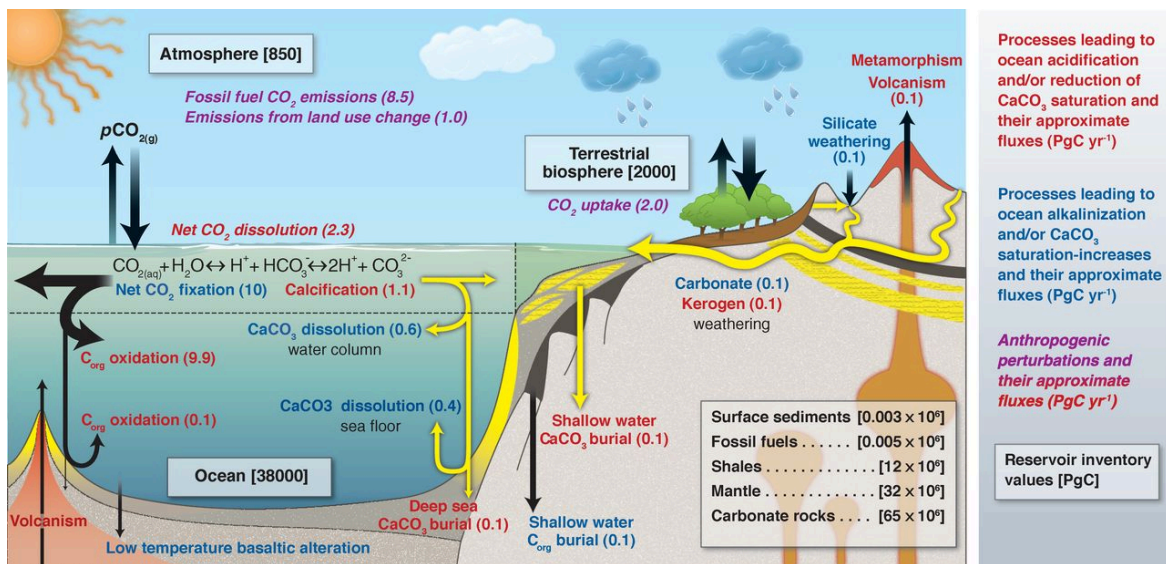
Figure 1.1 Marine carbon cycling in atmosphere, ocean and terrestrial biosphere (Hönisch et al., 2012). The atmospheric CO_2 dissolves in seawater and transform to bicarbonate, carbonate, and hydrogen ion. This process illustrates the water have high CO_2 absorbing capacity which introduces the ocean as the largest carbon reservoir.
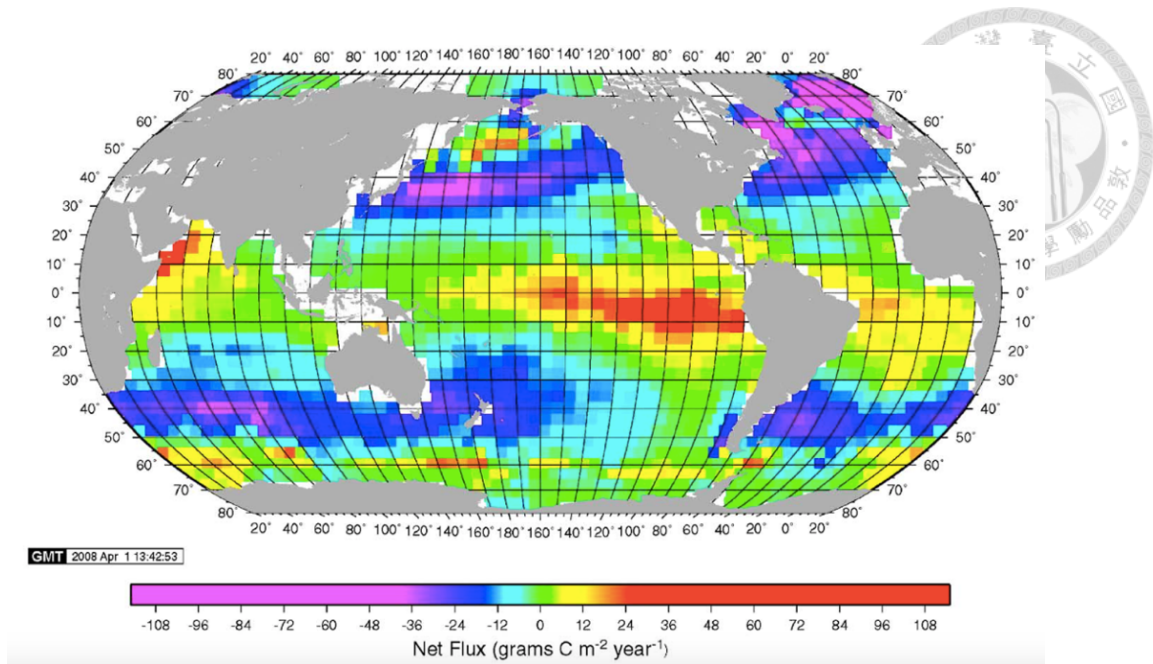
Figure 1.2 Climatological mean annual sea–air CO_2 flux for the reference year 2000 (g-C m^{-2} yr^{-1}) (Takahashi et al., 2009). For open ocean, the eastern equatorial pacific is the significant CO_2 source and mid-latitude regions is CO_2 sink.

1.2 Marine carbonate system

Ocean is the most important component of the global carbon cycle due to its role as the largest carbon reservoir on Earth. Seawater absorbs atmospheric CO_2 and the subsequent equilibrium reactions form a complex chemical system involving various biogeochemical processes.

In the ocean, carbon dioxide exists in three major inorganic forms: aqueous carbon dioxide ($CO_{2(aq)}$), bicarbonate (HCO_3^-) and carbonate ion (CO_3^{2-}), and their relative abundances in seawater are as a function of oceanic pH value (Fig 1.3). The true carbonic acid (H_2CO_3) is relatively smaller than $CO_{2(aq)}$ and these two species are analytically indistinguishable. Therefore, $H_2CO_3^*$ is refers to the sum of these two compounds. For gaseous $CO_{2(aq)}$, the dissolved concentration into surface seawater is controlled by

3

thermodynamic equilibrium, which is directly proportional to the atmospheric partial pressure of CO_2 (pCO_2) and illustrated by Henry's law:

$$CO_{2(g)} \overset{K_0}{\Leftrightarrow} CO_2 \, , \quad [CO_2] = K_0(T, S) * pCO_2 \qquad (1.1)$$
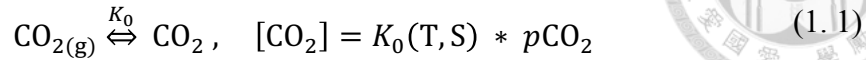
where K_0 is the solubility coefficient of CO_2 in seawater, and is a function of temperature (T) at constant salinity (S).

The carbonate species of dissolved CO_2 are related by the following equilibria:

$$CO_2 + H_2O \overset{K_1}{\Leftrightarrow} HCO_3^- + H^+ \overset{K_2}{\Leftrightarrow} CO_3^{2-} + 2H^+ \qquad (1.2)$$
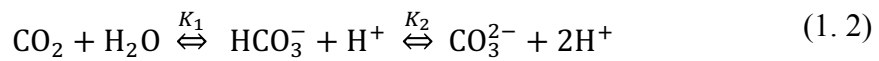
where K_1 and K_2 are stoichiometric equilibrium constants, often referred to as the first and second dissociation constants of carbonic acid, respectively. This equation shows that CO_2 dissociates into ionic species rather than merely physically dissolving, which is also recognized as the reason why CO_2 is more dissolved than other abundant gases in seawater.

Equilibrium in systems are illustrated from two perspectives: mass balance and charge balance, with the concept of Dissolved Inorganic Carbon (DIC) derived from the former and alkalinity from the latter for marine carbonate systems. DIC constitutes the basis of the carbonate system in seawater, defined as the sum of the concentrations of the species:

$$DIC \equiv \Sigma CO_2 = [CO_2] + [HCO_3^-] + [CO_3^{2-}] \qquad (1.3)$$

On the other hand, Total Alkalinity (TA) represents the buffer capacity or charge balance of seawater. .

$$TA = [HCO_3^-] + 2[CO_3^{2-}] + [B(OH)_4^-] + [OH^-] - [H^+] \pm \text{minor constituents} \qquad (1.4)$$

For regular used in carbonate system, carbonate alkalinity (CA) is replaceable of TA and simplified as followed:

$$CA = [HCO_3^-] + 2[CO_3^{2-}] \qquad (1.5)$$

4
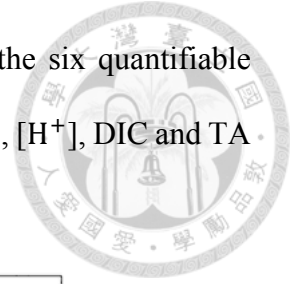
The marine carbonate system can be determined by any two of the six quantifiable variables ($[CO_2]$, $[HCO_3^-]$, $[CO_3^{2-}]$, $[H^+]$, DIC, TA). However, only $[CO_2]$, $[H^+]$, DIC and TA can be measured directly
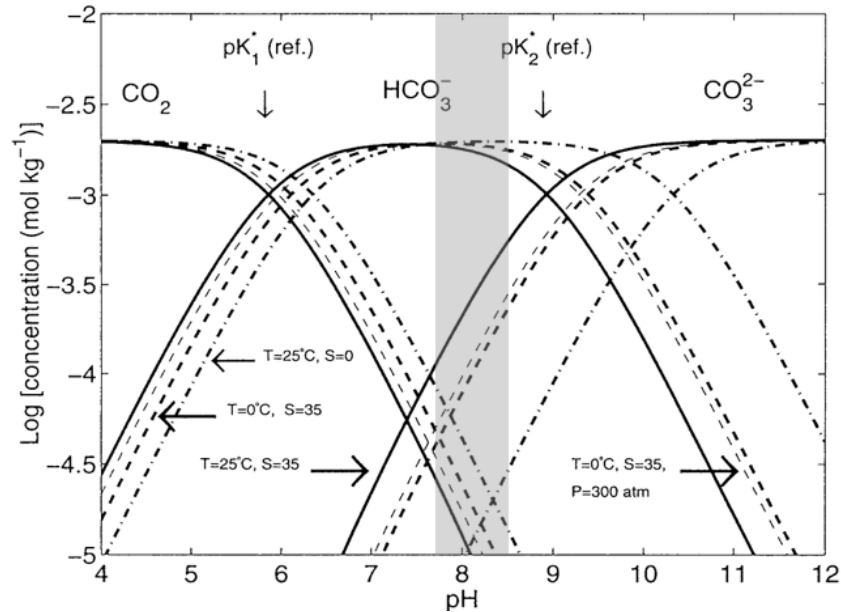
Figure 1.3 Carbonate system in Bjerrum plot. The grey area is oceanic pH range (modified from Zeebe and Wolf-Gladrow, 2001).

In order to better understanding the distribution of surface pCO$_2$, the pCO$_2$ can be described as followed:

$$pCO_2 \approx \frac{K_2}{K_0 \cdot K_1} \frac{(2 \cdot DIC - Alk)^2}{Alk - DIC} \tag{1.6}$$

According to Sarmiento (2013), the surface pCO$_2$ is controlled by three mechanisms from the biogeochemical perspective, including one physical and two biological processes:

(1) Gas exchange pump

The surface ocean pCO$_2$ is influenced by water temperature, DIC and Alk variations. As ocean is considered as a rapid gas exchange system, oceanic pCO$_2$ is in equilibrium with atmospheric pCO$_2$. Among these three parameters, DIC is the most

5
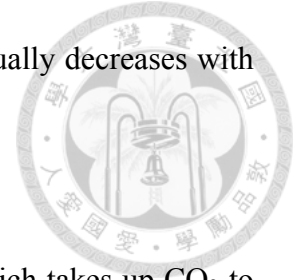
important parameter to maintain the chemical equilibrium, and usually decreases with increasing temperature.

(2) Soft-tissue pump

The most important biological reaction is photosynthesis, which takes up CO_2 to form organic matter (Eq 1.7), and then exports to the deeper ocean through settling particles or advection of dissolved organic carbon. This process leads to a transformation of inorganic carbon from surface into organic carbon then down to deep ocean.

$$106CO_2 + 16NO_3^- + HPO_4^{2-} + 78H_2O + 18H^+ \rightleftharpoons C_{106}H_{175}O_{42}N_{16}P + 150O_2 \qquad (1.7)$$
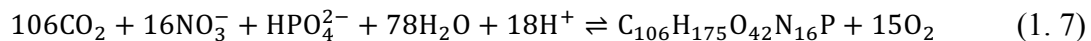
(3) Carbonate pump

The formation of biogenic carbonates (i.e., calcite or aragonite) (Eq 1.8) can be attributed to carbon cycling and the effect on Alk is twice than DIC. The shells of marine organisms, such as foraminifera, form calcium carbonates in the surface ocean. The dissolution of these shells in the deeper part of the ocean will cause the downward transport of Alk and DIC from the surface into the abyss.

$$Ca^{2+} + CO_3^{2-} \rightleftharpoons CaCO_3 \qquad (1.8)$$

1.3 Trace elements

1.3.1 Trace elements in Foraminiferal shells

For paleoceanographic and paleoclimate studies, the trace element (TE) composition in foraminiferal shell is a powerful tool for recording environmental variables in the past, such as temperature, salinity and seawater pH. When these environmental parameters changed through geological time, the trace element ratios in foraminiferal shell would co-vary in

6

response to the environmental changes. Hence, measuring the shell chemistry enables us to track the environment change in the past.

The relationship between shell composition and seawater is expressed by an empirical partition coefficient (D):

$$\left.[TE]\middle/[Ca]\right._{\text{foraminifer shell}} = D \times \left.[TE]\middle/[Ca]\right._{\text{seawater}} \tag{1.9}$$

According to the thermodynamic consideration, the distribution constant (K) can be obtained from the reaction below:

$$CaCO_3 + TE^{2+} \rightleftharpoons TECO_3 + Ca^{2+} \tag{1.10}$$
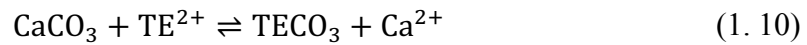
$$K = \frac{[CaCO_3][TE^{2+}]}{[TECO_3][Ca^{2+}]} \tag{1.11}$$

Particularly, the utilizing of TEs in marine carbonates is followed by D rather than thermodynamic-based K. This emphasized the strong biological control over the uptake of TE in living organisms. As a result, the shell chemistry in foraminifera reflects combined information of physical (thermodynamic) and biological (kinetic) processes during the shell formation.

However, different species behave differently under various environmental conditions. Evaluating the mechanism for TEs incorporations is rather challenging, the term "vital effect" is, therefore, used for any biological responses. In this view, the determination of D is required by empirical calibrations for different marine organisms.

Abundances of trace elements in foraminiferal shells are summarized in Figure 1.4 (Lea, 1999). For elements Mg, Na, Sr and F, the abundances are greater than 10^{-3} mol/mol Ca (so called "minor elements"). Abundances of elements B, Li, Mn, Zn and Ba are range from 10^{-}

7

[3]-10[-6] mol/mol Ca, and other elements (Fe Cu, Nd, Cd, V, U) are presented at abundances between 10^{-6}-10^{-9} mol/mol Ca.

With the empirical calibrations from culture and core-top specimens, TE/Ca ratios have been widely used to reconstruct the paleo-environment. According to Lea (1999), TE/Ca ratios can be classified into four groups by their applications: (1) Nutrient proxy (Cd/Ca, Ba/Ca): record seawater nutrient levels; (2) Physical proxy (Mg/Ca, Sr/Ca, B/Ca): record physical parameters (temperature, pressure and pH); (3) Chemical proxy (Li/Ca, U/Ca, Sr/Ca, Nd/Ca): record ocean chemistry; (4) Diagenetic proxy (Mn/Ca, Fe/Ca): record post-depositional signals. However, it needs to use in caution as many of these TE/Ca ratios are often influenced by more than one environmental variable.

In this study, Mg/Ca and Ba/Ca are used as proxies for sea surface temperature and upwelling intensity, respectively. The background information on these two proxies are further provided in the following sections.
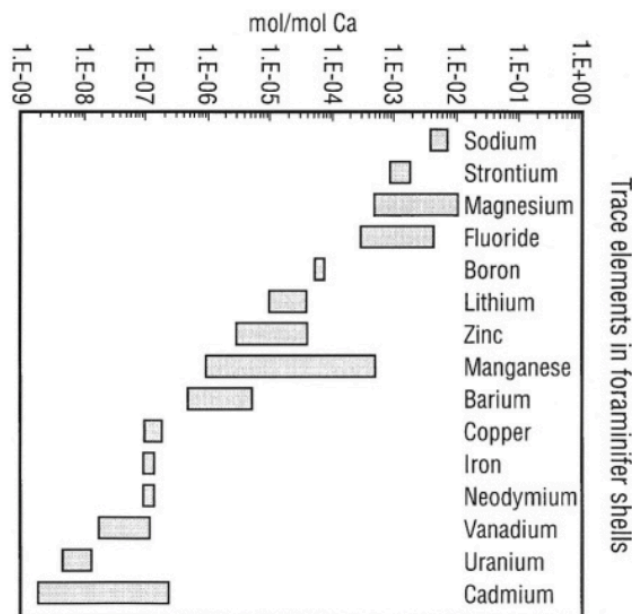
Figure 1.4   Trace element abundances in foraminifera shells (mmole/mol Ca) (Lea, 1999).

8
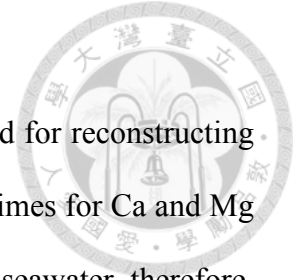
1.3.2 Mg/Ca proxy

Planktonic foraminiferal Mg/Ca thermometry has been widely used for reconstructing past change in Sea Surface Temperature (SST). The oceanic residence times for Ca and Mg are relatively long (10^6 and 10^7 years, respectively), the Mg/Ca ratio of seawater, therefore, can be considered as constant at the glacial/interglacial timescales.

The thermodynamic equilibrium predicted that the incorporation of Mg into calcite is about +3% per K(Lea et al., 1999). For the empirical calibrations of the Mg/Ca thermometry, they are mainly based on three approaches: (1) culture experiments (Fig 1.5 (a)); (2) sediment trap (Fig 1.5 (b)) and (3) core tops (Fig 1.5 (c)). The calibration can be expressed as an exponential equation:

$$\frac{Mg}{Ca} \, (mmol\,mol^{-1}) = B \times exp(A \times T) \tag{1.12}$$

where T is the calcification temperature (℃). A and B are the exponential and pre-exponential constants, respectively. In most of the published work, A is often assumed to be 0.090, and B is species-specific.

For planktonic foraminifera, the size effect is an apparent feature for Mg/Ca ratios (Elderfield et al., 2002). By increasing the test size, an increase in Mg/Ca is observed over several species of foraminifera (Fig 1.6). Therefore, the restriction on size is essential. Other intra-species variability in Mg/Ca ratios may due to the (1) biomineralization and (2) the formation of secondary crusts. Bentov et al. (2009) suggested that foraminifera actively remove Mg from the calcification fluid via fluid phase endocytosis. In addition, a series of high/low Mg bands are observed in shell calcites and represent the night/day variation, which can be linked to the Mg uptake by mitochondria (Spero et al., 2015). These observations further emphasize the role of biomineralization process for Mg uptake. Some planktonic

9

species can add an outer calcite crust prior to reproduction at depths significantly deeper and colder than their principal habitat depth. This gemetogenic crust can be account for up to 30% of the test weight in the case of *G. sacculifer* (Bé, 1980). In addition, inter-species Mg/Ca variability is generally controlled by calcification depth. Mix-layer dwellers contain high Mg/Ca ratios (e.g. *G. ruber*, *G. sacculifer*), whereas deep dwelling species have low Mg/Ca ratios (e.g. *N.dutertrei*, *P. obliquiloculata*). This may provide an approach to reconstruct the thermal structure of the water column.

However, there are several other factors that may bias the SST reconstructions using the foraminiferal Mg/Ca ratio. The culture studies illustrated the Mg/Ca increase with salinity, decrease with seawater pH and [CO_3^{2-}] (e.g. Russell et al., 2004). But for *G. sacculifer*, the effects of carbonate parameters are expected to be negligible (Allen et al., 2016). Core-top data show a systematic decrease in Mg/Ca ratio for planktonic foraminifera with increasing depth through partial dissolution under the influence of undersaturated waters (Huang et al., 2008; Rosenthal et al., 2000). This phenomenon is thought to be the preferential dissolution of high-Mg calcite of the test, and thus decreases the bulk Mg/Ca ratio and shifts the temperature estimates toward colder values.
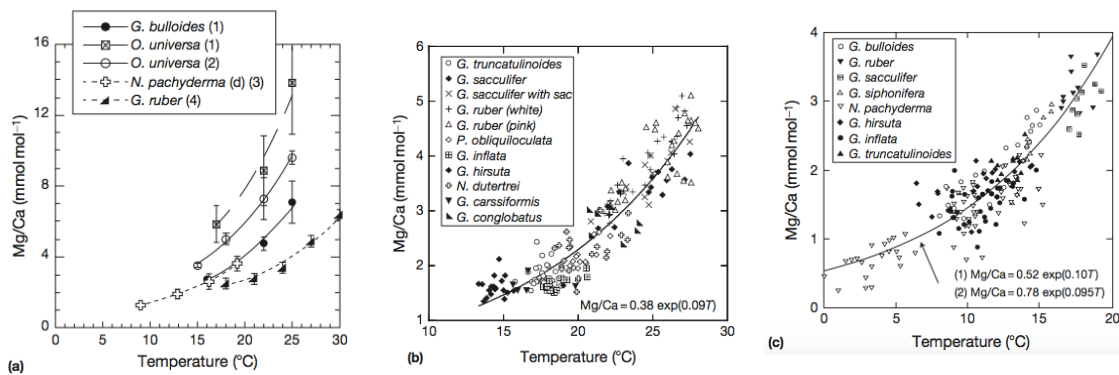
Figure 1.5 Mg/Ca-temperature calibration based on several published data (Rosenthal and Linsley, 2006). (a)culture experiments (e.g. Lea et al., 1999); (b)sediment trap (Anand et al., 2003); (c)core tops (Elderfield and Ganssen, 2000).

10
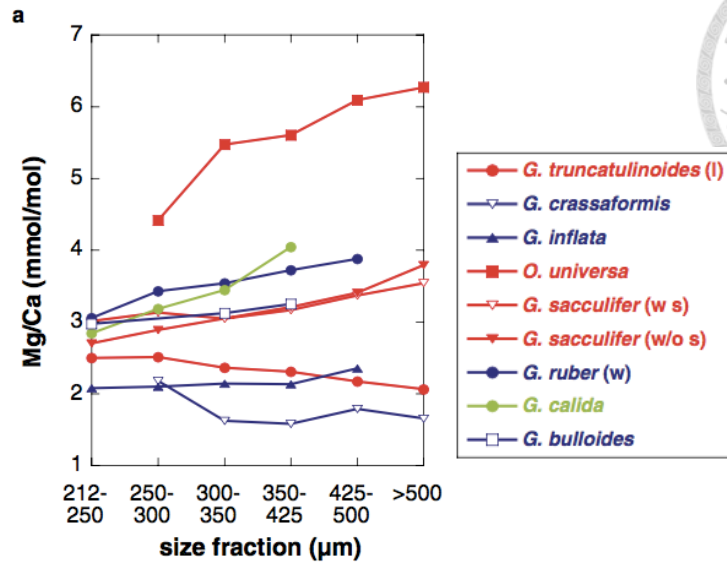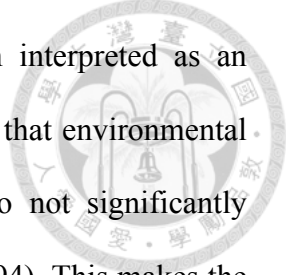
Figure 1.6 The Mg/Ca ratios versus size fraction of foraminifera (Elderfield et al., 2002). For *G. sacculifer*, the test size increase from 212 to >500μm may cause the shell Mg/Ca increasing from 3.01 to 3.54mmol/mol (~16% of the mean value).

1.3.3 Ba/Ca proxy

In the modern ocean, the dissolved Barium (Ba) exhibits a nutrient-type distribution in the water column, which is similar to alkalinity and silicic acid. Ba is depleted in the surface water and increase with depth due to remineralization. Ba is classified as bio-intermediate element (Libes, 2011). The fraction removed as particles from the surface but with a greater proportion of the particulate barium than biolimiting element. The abiotic formation of a particulate phase is comprised of the mineral barite ($BaSO_4$), where the Ba is mainly from the dissolution of siliceous and celestite ($SrSO_4$) tests deposited by radiolarians. The residence time of Ba is nearly 9,000 years (Broecker and Peng, 1982) due to the barite formation and the its concentration ranges from 30×10^{-9} to 150×10^{-9} mol/kg (Ostlund, 1987). Accordingly, Ba is related to the biogeochemical cycling.

11

Barium-Calcium ratio (Ba/Ca) of foraminiferal calcite has been interpreted as an indicator of the seawater Ba concentration. The culture studies suggest that environmental parameters such as salinity, temperature, pH, alkalinity and light do not significantly influence the Ba incorporation (Hönisch et al., 2011; Lea and Spero, 1994). This makes the Ba/Ca ratio a reliable proxy for reconstructing river run-off and sea surface salinity (e.g. Bahr et al., 2013; Hall and Chan, 2004). Another application is to reconstruct the past changes in upwelling intensity, which indirectly reflects the primary productivity in the ocean (e.g. Lea and Boyle, 1991).

For the partition coefficient (D_{Ba}) obtained from the culture experiments, the D_{Ba} is 0.15 ± 0.05 for *O. universa*, *G. ruber* and *G. sacculifer* (Hönisch et al., 2011) and agrees well with the previously reported D_{Ba} of 0.147 ± 0.004 for *G. sacculifer* and *O. universa* (Lea and Spero, 1994). Therefore, seawater Ba/Ca ratios can be estimated from foraminiferal Ba/Ca ratios using the following equation (Eq 1.13):

$$\frac{Ba}{Ca_{shell}} = 0.149(\pm 0.05) \times \frac{Ba}{Ca_{seawater}} \qquad (1.13)$$

No specie-specific difference is detected for the Ba incorporation. In addition, Ba is preferentially incorporated into the orthorhombic structure rather than rhombohedral structure because of its larger ionic radius relative to Ca. This leads to a small (<1) partition coefficient for Ba.
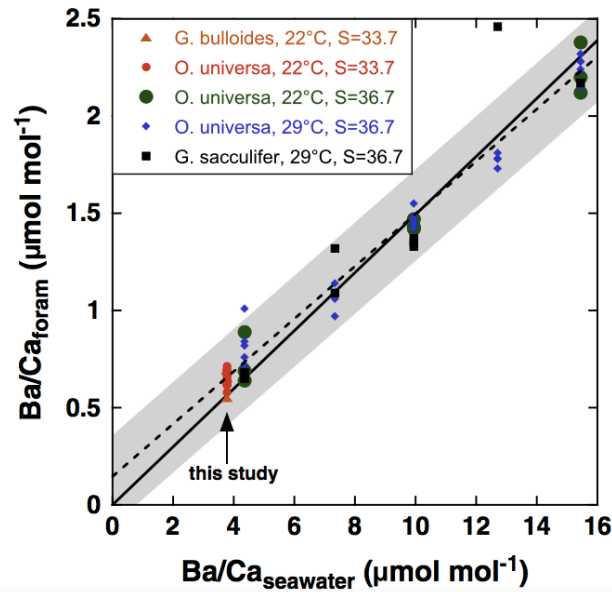
Figure 1.7 Ba/Ca ratios in shells of cultured *O. universa*, *G. sacculifer* and *G. bulloides* relative to the Ba/Ca ratio of experimental seawater (Hönisch et al. (2011) and references therein).

1.4 Boron isotope system

1.4.1 Boron and boron isotopic compositions

Boron predominantly exists in seawater as two species: the trigonally-coordinated boric acid $B(OH)_3$ and the tetrahedrally-coordinated borate ion $B(OH)_4^-$ (Fig 1.8). Although boron also presents as polynuclear forms at typical seawater pH, this amount can be negligible under normal seawater boron concentrations (Su and Suarez, 1995).
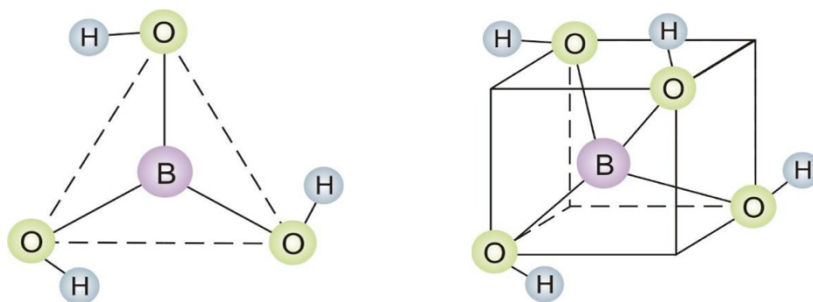
Figure 1.8 Tetrahedral complexes of borate ion ($B(OH)_4^-$) and trigonal complex of boric acid ($B(OH)_3$)

13
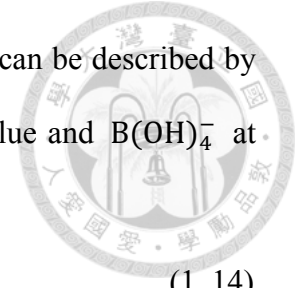
The relative proportion of these two species is pH-dependent and can be described by the Eq 1.14, showing that boron tends to form $B(OH)_3$ at low pH value and $B(OH)_4^-$ at high pH value.

$$B(OH)_3 + 2H_2O \rightleftharpoons B(OH)_4^- + H_3O^+ \tag{1.14}$$
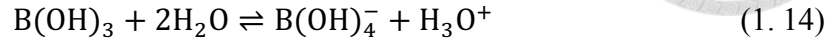
The disassociation constant of boric acid (pK_B^*) is nearly 8.6 in seawater (25℃, 35psu, and atmospheric pressure) and the temperature has a minor influence on pK_B^* (Dickson, 1990).

Boron has two stable isotopes, ^{11}B and ^{10}B, with relative abundances 80.18% and 19.82% of the total boron, respectively (IUPAC, 1998), and the isotopic variation is commonly reported using the delta notation.

$$\delta^{11}B \text{ (in ‰)} = \left[\frac{^{11}B/^{10}B_{sample}}{^{11}B/^{10}B_{standard}} - 1\right] \times 1000 \tag{1.15}$$

The standard used in equation 1.12 is National Institute of Standards and Technology (NIST) Standard Reference Material (SRM) 951 boric acid ($^{11}B/^{10}B=4.04367$) (Catanzaro, 1970).

The differences between these two chemical forms in coordination and vibrational frequency will cause the isotopic fractionation and can be described as the following isotope exchange reaction, where ^{10}B preferentially enters tetrahedral structure, $B(OH)_4^-$.

$$^{10}B(OH)_3 + {}^{11}B(OH)_4^- \rightleftharpoons {}^{11}B(OH)_3 + {}^{10}B(OH)_4^- \tag{1.16}$$
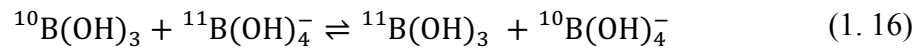
The equilibrium constant $^{11-10}K_B$ is given as:

$$^{11-10}K_B = \frac{^{11}B(OH)_3 \times {}^{10}B(OH)_4^-}{^{10}B(OH)_3 \times {}^{11}B(OH)_4^-} \tag{1.17}$$

The behavior of the boron in seawater ($[B]_{sw}$) is conservative though the distribution between $B(OH)_3$ and $B(OH)_4^-$ varies in the ocean (Lee et al., 2010). The isotopic composition of total boron in seawater ($\delta^{11}B_{sw}$) is 39.61±0.04‰ (Foster et al., 2010).

14
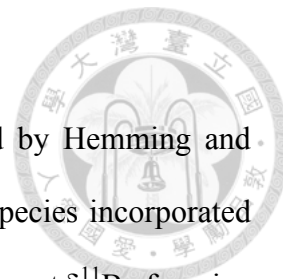
1.4.2 δ^{11}B -pH proxy – thermodynamic approach

The first model for boron incorporation into $CaCO_3$ is proposed by Hemming and Hanson (1992). They suggested that the borate ion is the only boron species incorporated into the growing surface of calcite or aragonite crystals since the measurement δ^{11}B of marine carbonates is close to the δ^{11}B of seawater $B(OH)_4^-$. Additionally, the length of the B-O bond (0.137 Å) is similar to that of the C-O bond (0.128 Å) (Kakihana and Kotaka, 1977), suggesting that borate ion substitutes directly for carbonate ion (Eq. 1.18).

$$CaCO_3 + B(OH)_4^- \rightarrow Ca(HBO_3) + HCO_3^- + H_2O \qquad (1.18)$$
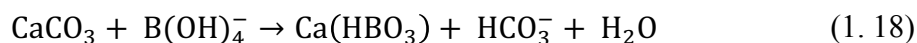
Based on this assumption, the seawater pH can be calculated from the measured δ^{11}B value of $CaCO_3$ using the Equation 1.16 with $\delta^{11}B_{sw}$, pK_B^* and α_B determined.

$$pH = pK_B^* - \log\left(-\frac{\delta^{11}B_{SW} - \delta^{11}B_{CaCO_3}}{\delta^{11}B_{SW} - \alpha_B\delta^{11}B_{CaCO_3} - 1000(\alpha_B - 1)}\right) \qquad (1.19)$$

Theoretically, δ^{11}B in $CaCO_3$ is the most reliable paleo-pH proxy, however, there is still an uncertainty when applied to the records beyond the residence time of boron in the oceans (10-20Ma) (Lemarchand et al., 2002; Simon et al., 2006).

1.4.3 δ^{11}B -pH proxy – biological control

The thermodynamic model provides a fundamental understanding of why boron isotopes in marine carbonates can be the most reliable proxy for seawater pH. However, biogenic carbonates that used for paleo-reconstructions are subject to physiological influences (e.g. Foster, 2008; Henehan et al., 2013), and thus, the caution should be taken when applying δ^{11}B in biogenic carbonates as a proxy for seawater pH (Fig 1.9). In the following section, we only focus on the utility of foraminiferal δ^{11}B.

The published δ^{11}B-pH calibrations show δ^{11}B in marine biogenic carbonate is highly correlated with aqueous pH value. Still, the discrepancies in pH sensitivity for aqueous δ^{11}B$_{borate}$ and measured δ^{11}B$_{CaCO3}$ between studies in inorganic calcite and foraminiferal calcite (using cultured, sediment-trap, and core-top specimens) are well observed. Therefore, a feasible approach for the pH reconstruction is to provide an empirical calibration for the foraminiferal species that are commonly used (Fig 1.10).

Three possible reasons for the offset between δ^{11}B$_{borate}$ and δ^{11}B$_{CaCO3}$: (1) Incorporation of boric acid (e.g. Noireaux et al., 2015); (2) Isotopic fractionation for the incorporation of borate ion (e.g. Pagani et al., 2005); (3) Change in chemistry or pH of the calcification fluid. The first two processes have been considered as the minor influence. For the third one, planktonic foraminifera can adjust the microenvironment for utilizing the essential elements in seawater. This calcification site is strongly influenced by physiological processes (Eq 1.20), but it is difficult to fully understand the biological influence on foraminiferal δ^{11}B based on the existing models (Fig 1.11, Zeebe et al., 1999).

$$Ca^{2+} + 2HCO_3^- \underset{Dissolution}{\overset{Calcification}{\Leftrightarrow}} CaCO_3 + H_2O + CO_2 \underset{Respiration}{\overset{Photosynthesis}{\Leftrightarrow}} CH_2O + O_2 \qquad (1.20)$$
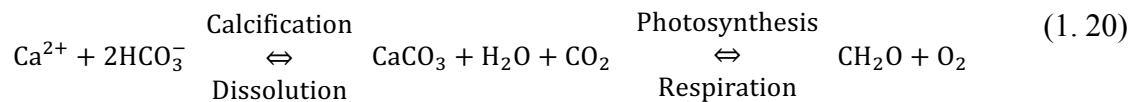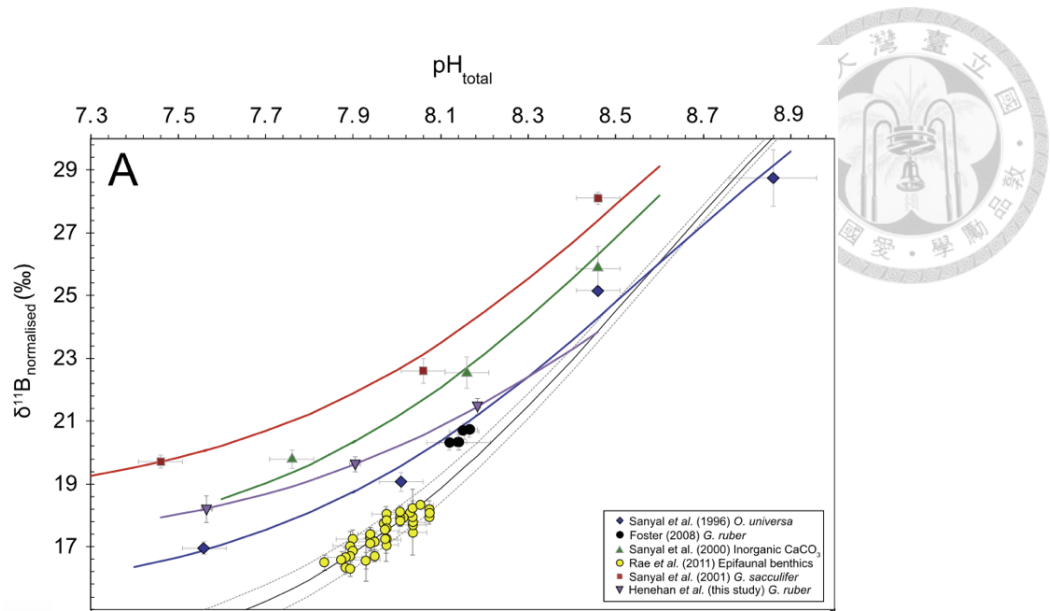
Figure 1.9 The boron isotopic composition compared to the pH of the water from published culture and inorganic precipitate data. The $\delta^{11}B$ is normalised to a $\delta^{11}B_{SW}=39.61‰$, 26 ℃ and 37.2 psu (Henehan et al., 2013).
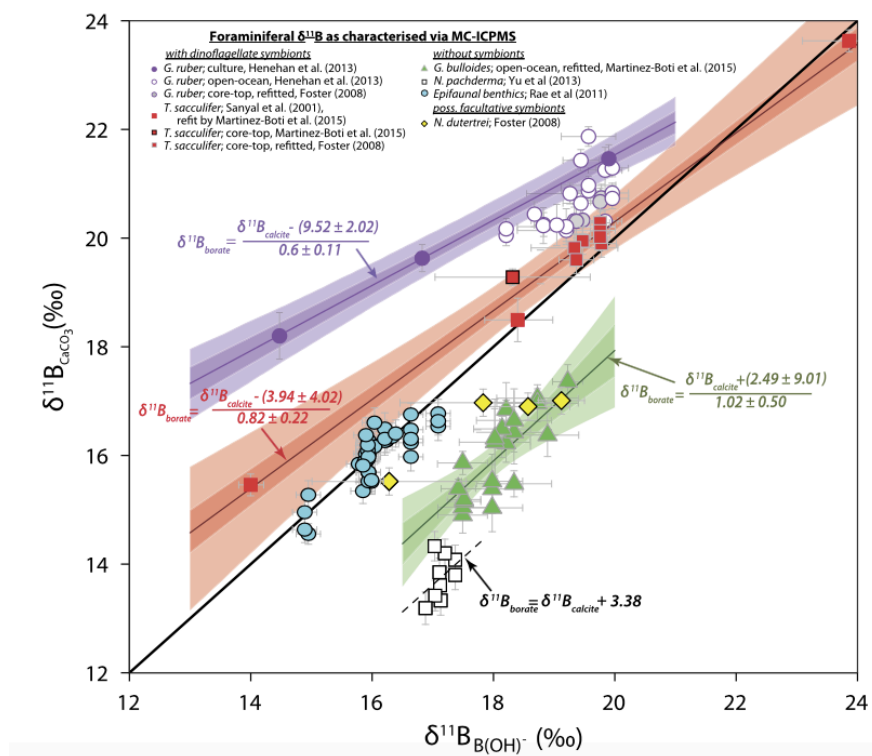
Figure 1.10 $\delta^{11}B$-pH calibrations for planktonic foraminifera by MC-ICP-MS measurements of solution (Henehan et al., 2016 and references therein). The *G. sacculifer* calibration (red) overlaps with 1:1 line, representing the most equilibrium species for boron isotopes.

17
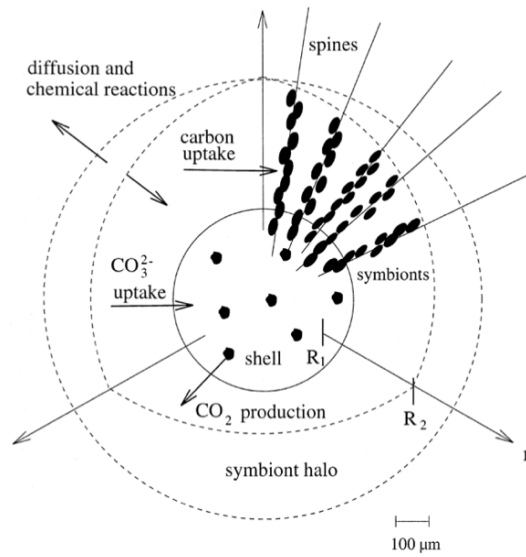
Figure 1.11 The diffusion-reaction model illustrates the microenvironments around planktonic foraminifera for carbonate system perturbation. Diffusive boundary layer is range from R_1(test edge) to r (over R_2, symbiont located) (Zeebe et al., 1999).

1.5 Aim of this study

During the last deglaciation, the open ocean has been recognized to regulate changes in atmospheric CO_2. The contribution from marginal sea, however, is still poorly constrained. Additionally, modern observations clearly demonstrate that marginal seas may also play a central role in controlling global air-sea CO_2 fluxes. Therefore, identify the role of marginal sea as a source or sink for atmospheric CO_2 in the past is of great importance.

As the largest marginal sea, the South China Sea (SCS) encompasses a variety of physical–biogeochemical domains in marine carbon cycle. The modern SCS serves as a weak or moderate source of atmospheric CO_2 with large seasonal/interannual variability (Dai et al., 2013; Tseng et al., 2007). In particular, the pCO_2 determination in the western SCS is similar to central basin, which can represent the exchange between surface water and atmosphere throughout the SCS (Zhai et al., 2013). Besides, the summer upwelling in the western SCS gives another opportunity to constrain the hydrological variability over the geological time scale. Combined with above advantages, the western SCS provides a unique site for paleoclimate studies.

This study utilizes the shell chemistry of planktonic foraminifera *G. sacculifer* from sediment core MD01-2904 in the western SCS to reconstruct the pact changes in surface ocean condition. Three geochemical/isotopic proxies are involved: Mg/Ca as a proxy of sea surface temperature; Ba/Ca as a proxy for upwelling intensity; and the boron isotopic composition as a proxy for the surface water pH. These results would provide new insights into changes in carbon cycle and hydrological properties in the marginal sea during the last deglaciation.

CHAPTER 2   STUDY AREA

2.1 Modern hydrography of South China Sea

The South China Sea (SCS) is a large semi-enclosed marginal ocean basin, extends from the equator to 23°N and from 99°E to 121°E with a total area of 3.5 million km^2 and an average depth of over 2000 m (Wang and Li, 2009). It is connected with the East China Sea to the northeast, the Pacific Ocean and the Sulu Sea to the east, and the Java Sea and the Indian Ocean to the southwest (Fig 2.1).

The climatic and hydrological features in the SCS are primarily controlled by the seasonally reversing East Asian monsoon (Wyrtki, 1961). In summer (June–August), the southwest East Asian summer monsoon (EASM) prevail over the southern basin and forms an anticyclonic circulation. In winter (December–February), the East Asian winter monsoon (EAWM) from northeast drives a cyclonic circulation in the entire SCS basin. The two anti-phase seasonal monsoons cause the offshore Ekman transport and further induces strong upwelling of cold, high nutrient waters at two regions, for summer in eastern Vietnam coast and for winter off the northwestern edge of the Philippines (e.g. Liu et al., 2002; Fig 2.2). The difference hydrographic properties between seasons is observed including sea surface temperature (SST) and salinity (SSS), productivity and upper water column structure of the SCS.

The thermocline in SCS reflecting the thermal evolution is affected by western Pacific warm pool and East Asian monsoon. The average depth of thermocline is thinnest in winter (100 m), thickest in spring (75 m), and transitional in summer and autumn (75–85 m). Its slope is opposite between season due to monsoon influence with the upper water piles up in

the northwestern part of the SCS in winter and in the southeastern part in summer (Liu et al., 2000).

Due to large inputs of terrigenous sediments in marginal sea, the SCS sedimentation rates are high (30-100 cm/ka, about an order of magnitude higher than the other parts of the Pacific). Furthermore, the carbonate compensation depth (CCD) in the SCS is nearly 3500 m (Wang and Li, 2009). With these two unique features, the SCS provides an ideal region for studying high-resolution paleoceanographic reconstructions.
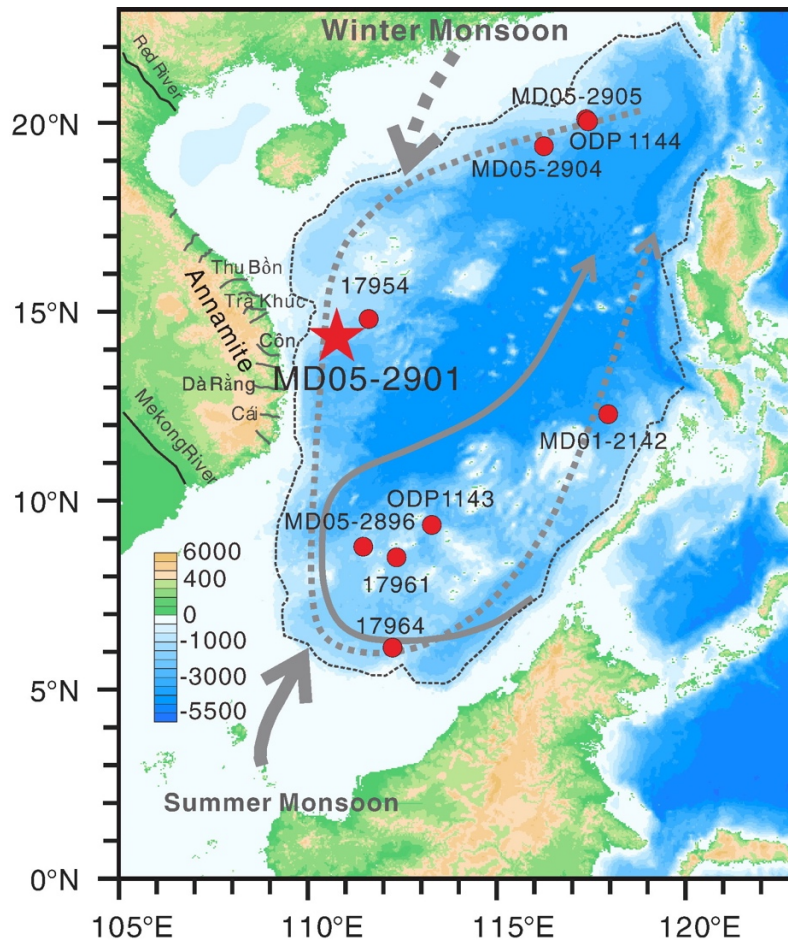
Figure 2.1   The South China Sea regional map shows the location of the studied core MD05-2901. The East Asian Summer Monsoon (gray solid line) and Winter Monsoon (gray dashed line) along with the modern monsoon-driven surface circulations are also plotted. The glacial shoreline is sketched as black dashed line (Li et al., 2015a).

21
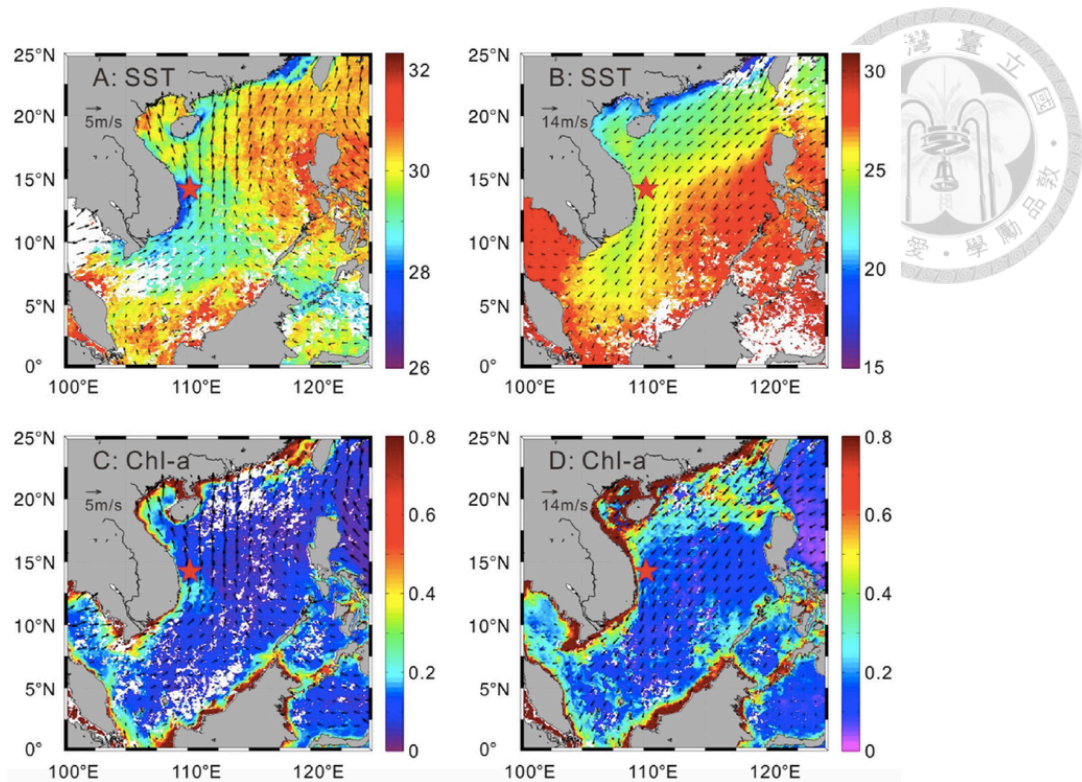
Figure 2.2 Modern oceanographic feature of the South China Sea, showing sea surface temperature in (a) summer and (b) winter and Chlorophyll-a concentration in (c) summer and (d) winter (Li et al., 2015b, data from NOAA).

2.2 Modern carbon cycle in South China Sea

Carbon cycling in the ocean can be divided into three systems, including air-sea interface, within the water column, and between bottom water and sediments. The first two aspects are included as follows:

(1) Air-sea CO2 interface

The interaction between surface seawater and atmosphere has a great impact on climate. For the biogeochemistry and the carbon reservoir of the SCS, two characteristics are described in Wang and Li (2009): (1) The monsoon-driven seasonal patterns in bio-productivity and nutrient dynamics distinguish the SCS from other low-

22

latitude waters; (2) The semi-enclosed nature of the SCS basin allows only limited exchanges with the western Pacific Ocean via an upper part exchange with the Kuroshio current and overflows at depth (e.g. Dai et al., 2013), and brings specific features into its basin-wise circulation and carbon cycling.

Moreover, the biological pump is an important mechanism controlling the surface pCO_2 (see Section 1.2). The pump efficiency can be illustrated by export of particulate organic matter (POM). For the carbon budget, the relationship between export of particulate organic carbon (POC) from the euphotic zone and the upwelled dissolved inorganic carbon (DIC) will control the pCO_2 absorption or the release from surface water to atmosphere. Based on the model study in the SCS, the modeled annual mean POC export flux is 1.95 mmol m^{-2} day^{-1}, which is much smaller than the total DIC flux of 7.93 mmol m^{-2} day^{-1} (Ma et al., 2014). Even though the modeled POC flux is strongly influenced by the East Asian Monsoon, this result indicated that surplus DIC from deep ocean is a predominant factor for surface pCO_2 over SCS.

The sea-air CO_2 fluxes in the western and central SCS in the field observation has provided the values ranging from 0.73 mmol m^{-2} d^{-1} in summer and 0.55 mmol m^{-2} d^{-1} in winter, which implied a very weak CO_2 source in these two seasons (Chen et al., 2006). However, a recent study suggests that the western and central SCS serve as a weak source of atmospheric CO_2, which is much higher than those reported in previous results (Zhai et al., 2013), showing that sea–air CO_2 fluxes range from 1.62 mmol m^{-2} d^{-1} in October to 8.35 mmol m^{-2} d^{-1} in August. The annual sea-air CO_2 flux in this region is estimated at 1.37 ± 0.55 mol m^{-2} d^{-1}, higher than the other areas in the SCS (Fig 2.3). This further suggests that the W-SCS is a very sensitive area for the sea-air CO_2 flux.
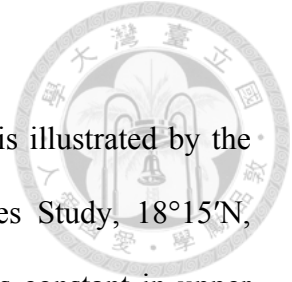
(2) Carbonate chemistry of seawater column

A typical depth distribution of dissolved carbon in the SCS is illustrated by the observational data at the SEATS (South-East Asian Time Series Study, 18°15′N, 115°35′E) station (Fig 2.4, Chou et al., 2007). The TCO_2 remains constant in upper 2000m, and nearly 30% of normalized TCO_2 in the deep waters is from organic decomposition, and the other is from carbonate dissolution. The degree of carbonate saturation for aragonite ($\Omega_{aragonite}$) and calcite ($\Omega_{calcite}$) decreases rapidly with depth in the upper 1,000 m due to the decrease of $[CO_3^{2-}]$. In addition, the saturation depth of aragonite is at ~600m, and for calcite, the depth places at 2500m (Fig 2.4).
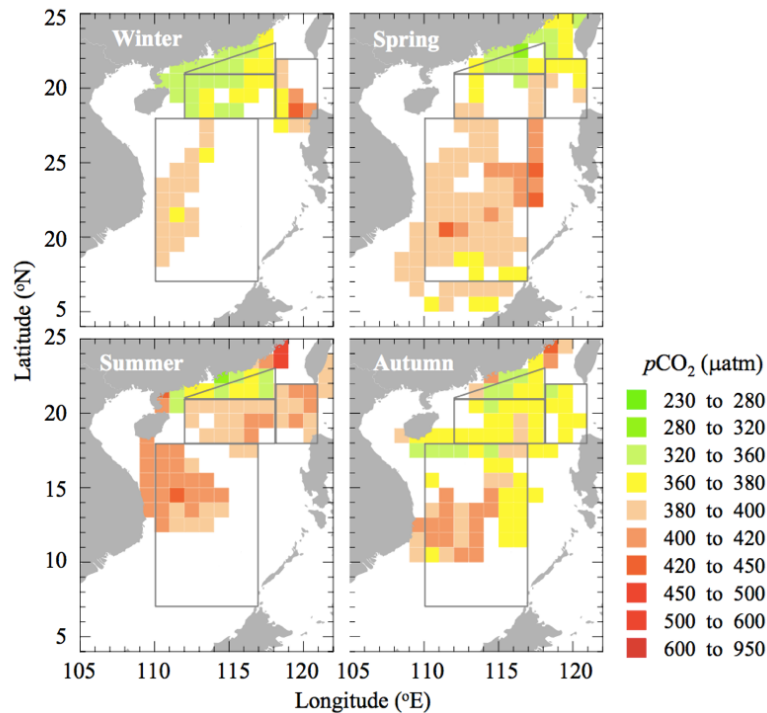
Figure 2.3 Sea surface *p*CO2 measurement in the SCS for seasonal distributions from October 2003 to April 2008 (Zhai et al., 2013).

24
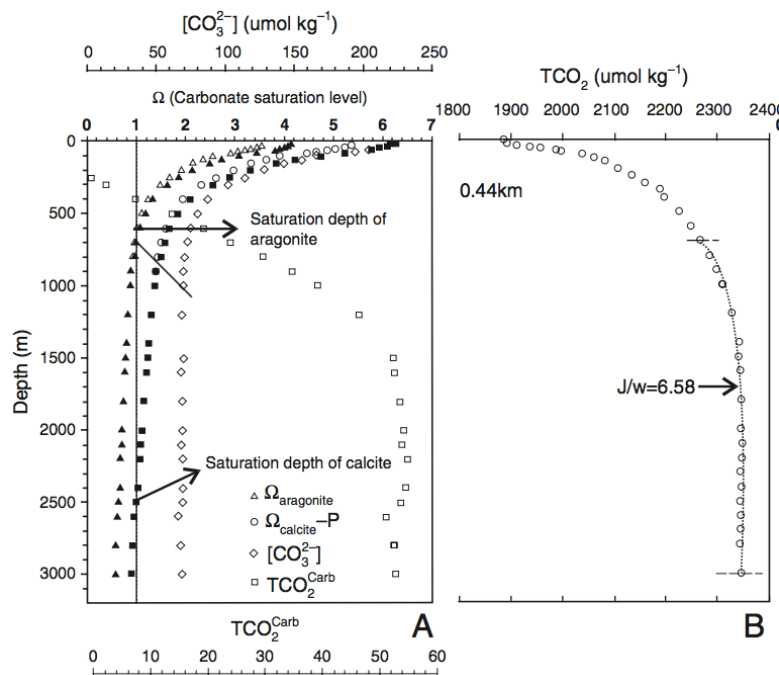
Figure 2.4 Depth profiles for carbon chemistry in SEATS station: (a) aragonite and calcite saturation levels along with concentration of carbonate ion; (b) TCO_2 variation (Chou et al., 2007).

25

CHAPTER 3   METHODOLOGY

3.1 Sample pre-treatment

3.1.1 Core sampling

Sediment core MD05-2901 (14°22.50′N, 110°44.60′E, water depth of 1454 m) in the W-SCS was selected and further investigated in the present work (Figure 2.1). This core was retrieved from the northeastern slope off Vietnam during IMAGE VII cruise of the R/V *Marion Dufresne* in 2005. The Calypso core length is 36.49 m and composed of homogeneous olive green or green gray clay sediments enriched with well-preserved calcareous and siliceous microfossils without obvious disturbance (Laj et al., 2005). The core is bathed above the present-day carbonate compensation depth (~3000 m) (Wang et al., 1999), and planktonic foraminiferal shells are abundant and well preserved. It has been sampled every 8 cm for the oxygen isotope, excluding the 1365–1435 cm interval because of shipboard coring disturbance.

The age model for core MD05-2901 was established mainly based on the oxygen isotopic stratigraphy by correlating the planktonic foraminifera δ^{18}O *Globigerinoides ruber* with the stack LR04 (Lisiecki and Raymo, 2005), and further constrained by two control-points: the last and the first appearance events of the pink *G. ruber* at 1273 cm (120 ka in age) and 3337 cm (404 ka in age), respectively (Li, 2007). Consequently, the bottom of core lies in marine isotope stage (MIS) 12 at an approximate age of 447 ka.

The foraminiferal samples are initially prepared in State Key Laboratory of Marine Geology, Tongji University (China). According to Wang and Li (2012), about 10 mL of wet core materials was used and washed by 63 μm sieve in order to remove fine sand. The coarse

fractions were then dried, underwent 154 μm sieve and nearly 300 well-preserved planktonic

foraminiferal shells were collected.
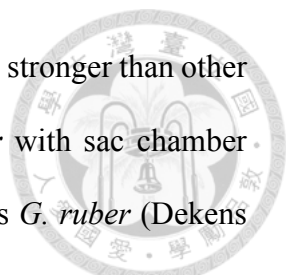
In the earlier work, core MD05-2901 has been studied for reconstructing the paleo-records over 270ka in the W-SCS, including (1) sea surface temperature based on planktonic foraminifera faunal assemblage, *G. ruber* Mg/Ca and alkenone $U_{37}^{k\prime}$ (Li et al., 2009; Wang and Li, 2012) (2) hydrological cycle based on n-alkane chain-length record (Li et al., 2015b) (3) primary productivity based on coccolithophorid assemblages (Su et al., 2013) and multi-algal lipids (Li et al., 2015a) (4) source provenance of clay minerals based on clay mineral composition (Liu et al., 2007). In this study, we focused on shell chemistry of planktonic foraminifera, *Globigerinoides sacculifer* for multi-proxy reconstructions over the last 22 kyr.

3.1.2 Selection of foraminiferal shell

The symbiont-bearing planktonic foraminiferal species *Globigerinoides sacculifer* is used in this study, which newly classified in *Trilobatus* (sensu Spezzaferri et al., 2015). The identification was referred to Schiebel and Hemleben (2017). About 30 individuals (1-2 mg) of *G. sacculifer* without sac-like final chamber were picked from the size fraction of 425–500 μm (Fig. 3.1). The reasons for these criteria are discussed below:

(1) Without sac-like chamber

The sac-like final chamber is a secondary crust of calcite at the time of gametogenesis, and is usually added at deeper depth in surface mixed layer (<50m) (Bé, 1977). This gametogenic calcite can account for up to 30% of the final test weight for *G. sacculifer* (Bé, 1980). In other words, the bulk analysis (with a sac-like final chamber) may contain more biological signal rather than the environmental condition.

The effect of gametogenic calcite on shell Mg/Ca ratios may be stronger than other TE proxies. The Mg/Ca-SST estimate indicates that *G. sacculifer* with sac chamber calcifies at greater depths compared to the surface-dwelling species *G. ruber* (Dekens et al., 2002; Rosenthal et al., 2000). Moreover, the Mg concentration in sac chamber is 3-4 times higher than other regular chambers under the same calcification temperature based on the results from the culture experiment (Nurnberg et al., 1996). For $\delta^{18}O$ and $\delta^{13}C$ data, there is no significant difference between *G. sacculifer* mixed-morphotype and *G. ruber* in the eastern equatorial Pacific (Martínez-Botí et al., 2015). In order to avoid any of the potential bias, only the *G. sacculifer* without a sac-like chamber was picked in this study.

(2) Size fraction (425–500 μm)

As stated above in Section 1.3.2, an increasing Mg/Ca in shell is observed by increasing the test size (Fig 1.6). This highlighted the important of size fraction controlling. For boron, the culture and core-top samples show that the boron isotope ratios in foraminifera increase with the shell size (Hönisch and Hemming, 2004; Ni et al., 2007). The $\delta^{11}B$ value in the size range of 515-865 μm is 2.2‰ heavier than that of 250-380 μm for *G. sacculifer* (Hönisch and Hemming, 2004). Moreover, previous studies demonstrate that this effect is possibly related to the depth of calcification. The smaller *G. sacculifer* dwells in the deeper water column where light and symbiont photosynthesis are limited along with lighter $\delta^{11}B$ in the shells (Figure 3.2(a)). Besides, the shells collected from the deeper water depth usually have lower size-normalized shell weights, indicating that dissolution may also influence the foraminiferal $\delta^{11}B$ value (Figure 3.2(b)). This might underestimate the reconstructed pH value for smaller size due to the slight slope at low pH in pH-$\delta^{11}B$ calibration equation. Therefore, for the

purpose of learning paleo-pH of the surface ocean, the shell size of *G. sacculifer* requires to be controlled in 425–500 μm without significant dissolution (. Here caution is raised when comparing data with previous studies, while *G. sacculifer* in the size range of 425–500 μm is not commonly used for paleoceanographic research.
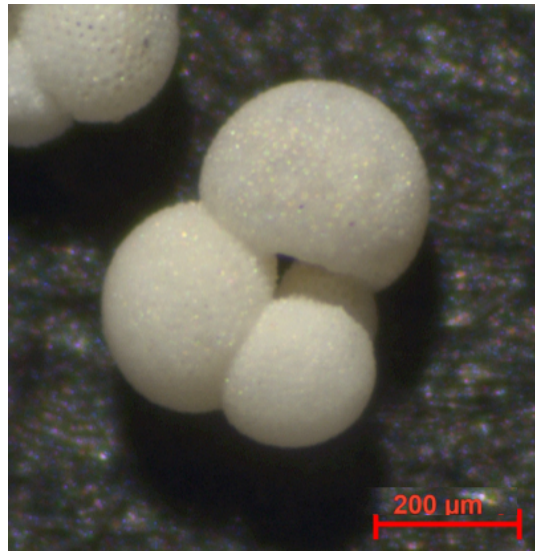
Figure 3.1   The sample selection of *G. sacculifer* under microscope.
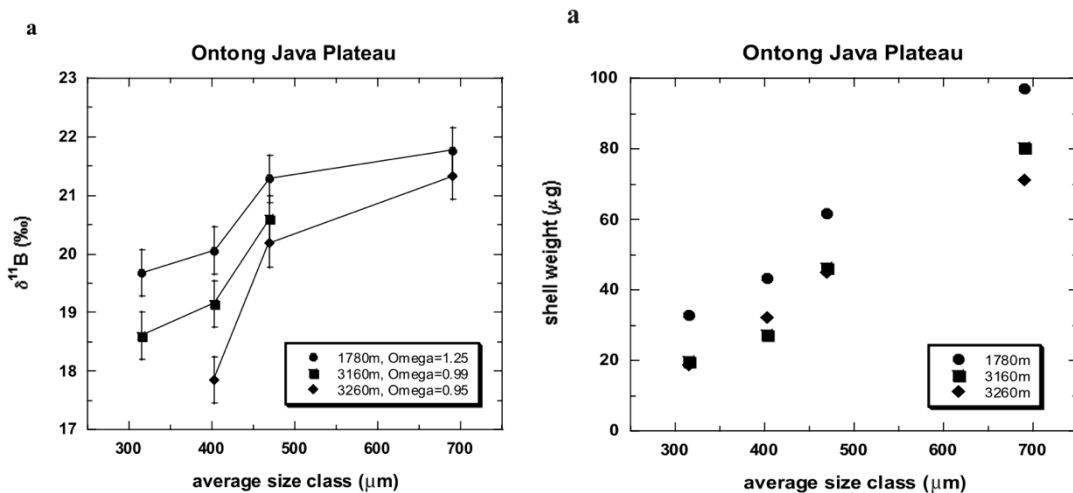
Figure 3.2   Shell size effect on δ^{11}B and the shell weight in *G. sacculifer* (Hönisch & Hemming, 2004).

29

3.1.3 Reagents and laboratory equipment

The sample preparation and the cleaning procedure were held at the Institute of Earth Sciences, Academic Sinica. High Efficiency Particulate Air (HEPA)-filtered class-10 laminar flow benches in a class-10000 clean room were utilized for this study and the boron purification is particularly operated in the boron-free clean room to achieve the low level of the boron blank. The boron-free clean room is equipped with, the boron-free Ultra Low Penetration Air (ULPA) filters because the standard HEPA filters contain ~10wt% borosilicate, which is considered to be the main contributor for the boron blank (varying from 10 to 40 pg) (Foster et al., 2006).

Ultrapure water is produced (resistivity 18.2MΩ at 25℃) by Milli-Q$^®$ Advantage A10 Water Purification System and the TOC value is controlled to be under 3 ppb. Only the PFA- and PP-containers are utilized in this study as the laboratory glassware usually contains significant amounts of boron. Ultrapure-grade (ULTREX Ⅱ, J.T. Baker) HNO_3 and HCl are used for chemical procedures and container cleaning in this study. For trace element analyses, the vials are washed with 1N HCl overnight, rinsed three times with DI water, and dried in the Class-10 flow bench before storage. Savillex PFA vials were cleaned on the Teflon-coated hotplate (at 150°C) with 8N HNO_3 and 6N HCl, and then fluxed with concentrated HNO_3 with trace HF before use.

3.1.4 Cleaning procedure for foraminiferal shell

The foraminiferal cleaning protocol for trace element analyses are adopted from the Cd- and Ba-cleaning methods developed by Boyle and Keigwin (1985), and Lea and Boyle (1991), relative to Mg-cleaning methods (Boyle, 1981). This cleaning protocol contains five

30

steps aimed to remove several contamination phases: (1) Fine clay removal (2) Reducing step (N$_2$H$_4$, remove metal oxides) (3) Oxidizing step (H$_2$O$_2$, remove organic matter) (4) Barite removal (DTPA) (5) Weak acid leaching. The overall cleaning steps involved in this study are as follows:
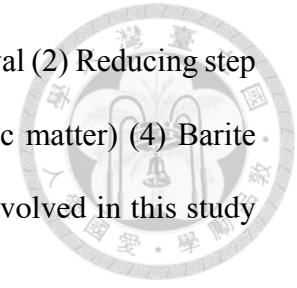
1. Sample preparation

   (1) 30 individuals (1-2 mg, 425–500 μm in size) of *G. sacculifer* without a sac-like final chamber were hand-picked under microscope, weighted and photographed for documentation.

2. Cleaning steps

   (2) Foraminiferal tests were crushed between clean glass slides to open the chambers and then transferred to 0.5 mL acid-cleaned PP microcentrifuge tubes.

   (3) The tests were ultrasonically cleaned three times with distilled water, twice with methanol and then rinsed with distilled water to remove fine clays and adhering detrital grains.

   (4) Reduction reagent (anhydrous hydrazine buffered with citric acid/ammonia and ammonium hydroxide solution) was used to remove Fe-Mn oxides.

   (5) Organic matter is oxidized with 0.3 % hydrogen peroxide-sodium hydroxide solution at 80°C for 10 minutes and the authigenic barite (BaSO$_4$) removal is done by adding 0.01M DTPA (buffered in 0.1N NaOH).

   (6) The final step is to remove adsorbed metals with dilute acid (0.065N HNO$_3$) and followed by distilled water to completely remove all surface-adsorbed and residual contaminants, and then transfer into new, acid-leached PP microcentrifuge tubes.

3. Sample Dissolution

   (7) After all these cleaning steps, the cleaned samples were dissolved in 100 μL of 0.3N

31

HNO$_3$, and then centrifuged for 10 min at 15,000 rpm. At this step, the upper solution will directly separate into two parts: 60 μL of sample solution for the boron isotope analysis and 30 μL of sample for trace elements determinations.
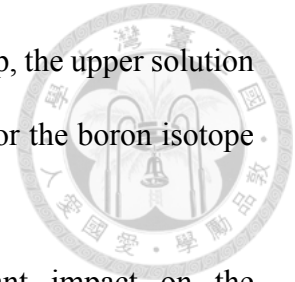
Notice that different cleaning procedure may have significant impact on the determination on trace element ratios determination (Yu et al., 2007). For Mg/Ca ratios determination, the cleaning protocol with the reductive step (the so-called "Cd method", used for the removals of Fe-Mn oxides) lower the shell Mg/Ca ratio compared to the "Mg method" (Barker et al., 2003; Rosenthal et al., 2004). There is a systematic offset between Cd method and Mg method by around 10% (Fig. 3.2). This offset can be attributed to the partial dissolution of foraminiferal shells when using hydrazine (Barker et al., 2003) or some other contaminating phase dissolution (Barker et al., 2005). Therefore, when comparing the paleo-SST records among different studies, the cleaning methods used in the studies should be checked with caution.
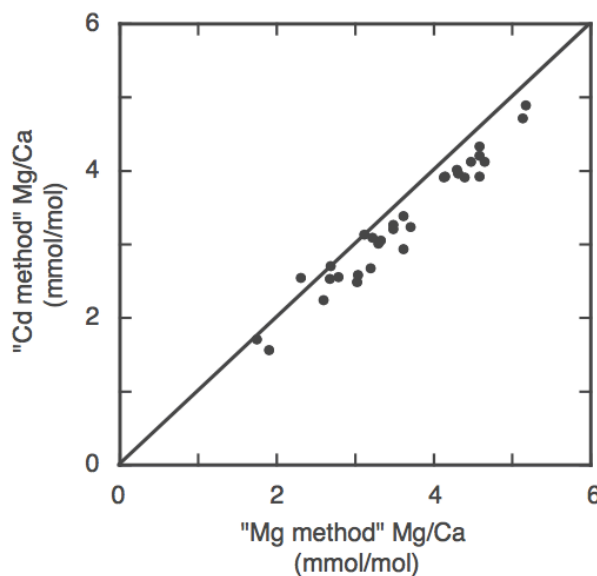
Figure 3.3 Comparison of Mg/Ca ratio between two cleaning procedure (Barker et al., 2005).

32

3.2 Sample dissolution and measurement procedure

G. sacculifer selection

1. Without a sac-like final chamber
2. 425–500 μm size fraction without test dissolution.
3. 30 individuals (1-2 mg)

↓

Foraminiferal cleaning protocol

1. Fine clay removal
2. Reducing step (N_2H_4, remove metal oxides)
3. Oxidizing step (H_2O_2, remove organic matter)
4. Barite removal (DTPA)
5. Weak acid leaching

↓

Dissolution

smaple dissoluted in 100 μL 0.1N HNO_3

↓ 60 μL solution   ↓ 30 μL solution

Micro-sublimation

HR-ICP-MS

Mg/Ca, Ba/Ca, Li/Ca, B/Ca,
U/Ca, Mn/Ca, Al/Ca, Fe/Ca

↓

MC-ICP-MS

Boron isotopes

3.3 Trace elements ratios measurement

3.3.1 Instrumentation (HR-ICP-MS)

Trace elements ratios in planktonic foraminifera were analyzed by a High-Resolution Inductively Coupled Plasma Mass Spectrometry (HR-ICP-MS, Thermo-Fisher Scientific™ ELEMENT XR) at Institute of Earth Sciences, Academia Sinica (IESAS) (Figure 3.3). The ELEMENT XR is a double-focusing mass spectrometer including an electromagnet sector and an electrostatic analyzer (ESA) for affecting the mass-/charge-dependent curvature and ion kinetic energy of ion trajectories, respectively (Nier-Johnson geometry). There are three detection modes for ELEMENT XR: Counting, Analog and Faraday mode. (Figure 3.3(b)). The dynamic range can be extended to 10^{12}.

For the introduction system used in this study, the stable sample introduction PFA spray chamber (Elemental Scientific, Inc.) coupled with PFA MicroFlow nebulizer (~100 µL/min, Elemental Scientific, Inc.) were selected. The standard sampler cone and X skimmer cone were applied. The details of instrumental parameters are listed in Table 3.1.

Figure 3.4　The high resolution inductively coupled plasma mass spectrometry (Thermo-Fisher ScientificTM ELEMENT XR) (a) Appearance (b) The detection system.
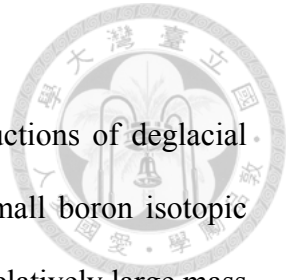
Table 3.1   Operating conditions for HR-ICP-MS.

parameters	Setting value
RF Power	1200 W
Fore Vaccum	$1.11 \times 10^{-3} \sim 1.52 \times 10^{-3}$ mbar
High Vaccum	$2.35 \times 10^{-7} \sim 3.06 \times 10^{-7}$ mbar
Sampling Gas Flow rate	$0.950 \sim 1.120$ L/min
Cooling Gas Flow rate	17 L/min
Auxiliary Gas Flow rate	0.87 L/min
Extraction voltage	-2000V
Nebulizer Type	PFA microflow 100μL/min
Peristaltic Pump Rate	8.75 rpm
Torch X-position	3.2mm
Torch Y-position	1.2 mm
Torch Z-position	-4.3 mm
Focus	$-850 \sim -900$ V
Shape	$190 \sim 200$ V

3.3.2 Trace element measurements

The foraminiferal TE/Ca ratios were simultaneously determined at the same detection mode to eliminate possible intensity bias and to quantify intensity ratios using external matrix-matched standards adapted from Rosenthal et al. (1999) and Huang et al. (2008). A series of matrix-matched standards (i.e., CS and SGS) were prepared from high-purity ICP standard solutions by a gravimetrical method and were standardize for TE/Ca by standard addition. Long-term reproducibility for Mg/Ca and Ba/Ca is evaluated by running the consistency standards and the matrix-matched standards during the analytical courses. External precisions (2SD, n= 30) are ±1.04% and ±1.55% for Mg/Ca and Ba/Ca, respectively. In addition, ^{27}Al, ^{55}Mn and ^{56}Fe were also measured by low and medium resolution to monitor detrital contaminants with the external precisions better than ±5% (2SD, n= 30).

3.4 Boron isotope measurement

Accurate and high-precision analysis is required for the reconstructions of deglacial seawater pH variability using the $\delta^{11}B$ in marine carbonates due to small boron isotopic variations (~2-4‰) in the ocean since the LGM. For the light isotopes, relatively large mass difference (~10% for boron) results in large isotope fractionations during natural processes and the measurements. A correction for instrumental mass fractionation is, therefore, necessary before obtaining the reliable information for the natural isotopic variation. For the boron isotope analysis, the standard-sample bracketing technique is applied to correct for the instrumental mass fractionation. On the other hand, limited sample sizes of marine biogenic carbonates combined with the low boron concentration make it difficult to achieve the high-precision measurements. This also sheds light to the importance of controlling the low procedure blank for boron. All the reasons above raise the difficulty for the boron isotope measurements.

For the instrumentation, three kinds of mass spectrometry are commonly used for the boron isotope analysis: positive thermal ionization mass spectrometry (P-TIMS), negative thermal ionization mass spectrometry (N-TIMS), and multi-collector inductively coupled plasma mass spectrometry (MC-ICPMS). With the improvement of the analytical performance (e.g., stability and sensitivity), MC-ICP-MS has been widely used for the high-precision (better than ± 0.50‰, 2SD) boron isotope measurements on biogenic carbonates nowadays. In this study, we have established an accurate and high-precision method on MC-ICP-MS for determining the boron isotopic compositions of foraminiferal shells.

3.4.1 Boron purification (micro-sublimation)

In order to obtain reliable $\delta^{11}B$ data, purification procedure is essential prior to the boron isotope measurements. Particularly, the instrumental mass fractionation on MC-ICP-MS can be significantly reduced and further corrected by introducing the target element prior to the isotopic analysis. Therefore, separating boron from original complex matrices is necessary.

There are two different strategies for the purification of boron: column chromatography and micro-sublimation. Column chromatography methods often use the boron-specific resin Amberlite IRA 743 (e.g. Foster, 2008; Kiss, 1988) or a series of mixed resins (e.g. Gaillardet and Allegre, 1995). The micro-sublimation technique, initially adapted from the purification step of osmium, has been applied to separate boron from the organic-rich matrices (Gaillardet et al., 2001). It can be used as an additional purification step after the ion exchange chromatography (Lemarchand et al., 2002) or a one-step separation method for Ca- and Na-rich matrices (Wang et al., 2010).

For marine biogenic carbonate, both column chromatography and the micro-sublimation method can achieve nearly 100% recovery (Hoecke et al., 2014). Applying the ion exchange resins often increases the procedure blank for boron during the column chemistry. The micro-sublimation method is relatively simple and significantly reduces the potential contaminations from the laboratory environment. In addition, the micro-sublimation technique provides further separation of boron from organic materials (e.g. organic matters in biogenic carbonate samples) and thus ensures the accurate and high-precision (better than 0.30‰, 2SD) boron isotope analysis (Gaillardet et al., 2001; Wang et al., 2010). Hence, the micro-sublimation technique is applied in this study and the detailed steps are as follows:
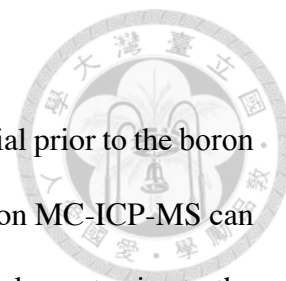
(1) After the cleaning procedure and sample dissolution, 60 μL sample solution is immediately loaded on the lid of a 5 mL Savillex® PFA conical vial.

(2) The beaker is screwed tightly and heated on a hotplate in the upside-down position at a constant temperature of 98°C for 12 hours (Fig 3.5).

(3) Switch off the hotplate and let the vial cools down under the room temperature.

(4) The final droplet (i.e. the boron fraction) is collected on the top of the vial, and adds 540 μL of 0.1N HNO_3.

(5) Finally, the final solution is transferred to a 2 mL PP centrifuge tube for the MC-ICP-MS measurement.
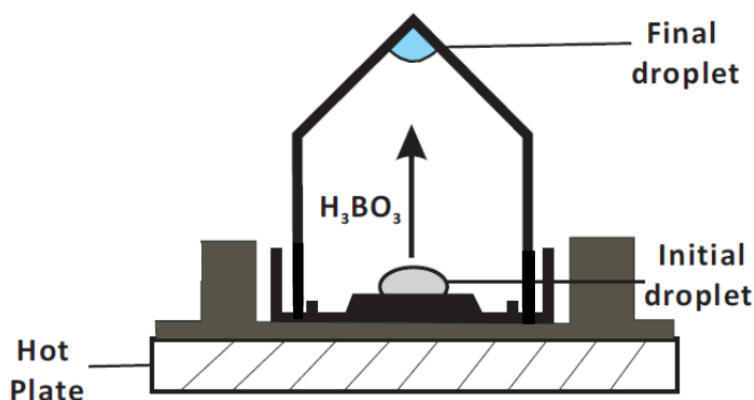
Figure 3.5 The schematic diagram of micro-sublimation technique.

3.4.2 Instrumentation (MC-ICP-MS)

The boron isotopic compositions were carried out on a High-Resolution Multi-Collector Inductively Coupled Plasma Mass Spectrometer (HR-MC-ICP-MS), Thermo-Fisher™ NEPTUNE *Plus*, at IESAS (Fig 3.6). The NEPTUNE *Plus* is a double-focusing MC-ICP-MS with high-sensitivity Jet Interface. This new generation HR-MC-ICP-MS enables us to measure limited sample size and obtains accurate and high-precision $\delta^{11}B$ data, which are

comparable to the traditional TIMS methods with additional advantages of requiring rather small amount- as low as 5 ng- of boron and facilitating high sample throughput.

The instrumental parameters used in this study are listed in Table 3.2. For the introduction system, the standard quartz spray chamber with a PFA-ST nebulizer (100 μL/min) is utilized in order to minimize the boron blank and the memory effect. The Ni Jet sampler cones and X skimmer cones were applied for enhancing the signal sensitivity. Analyses were performed on 0.1N HNO_3 solution with boron concentration of 10 ng ml^{-1}, typically yielding a ^{11}B ion beam of 3-4 x 10^{-11} A ($10^{11}\Omega$ resistor) at the uptake rate of ~100 μL/min. Compared with existing MC-ICP-MS methods, adding ammonia gas/solution is not necessary as the memory effect is negligible during the analytical courses.

To achieve accurate and high-precision isotope analyses, the tuning parameters are adjusted by two additional steps: (1) optimizing the signal sensitivity and stability; and (2) tuning the sample gas to obtain the most stable isotope ratios. The most stable condition for the boron isotope measurements on Neptune MC-ICP-MS can only be achieved if the sample gas is tuned daily for the stability of isotopic ratios rather than the optimal sensitivity (Foster, 2008).

The signal intensities of ^{11}B and ^{10}B were measured simultaneously on H3 and L3 Faraday cups, respectively. Sample uptake prior to data acquisition was 35 s, and then off-peak baseline and automatic peak center were performed. The analytical protocol involved the acquisition of 60 cycles (6 blocks/10 cycles) with the integration time of 1.324 s per cycle (Idle time: 1.000 s). The total data acquisition time did not exceed 3 min, followed by a 120s wash time with 0.1N HNO_3, and no significant memory effect were detected in this study. The sequence (shown in Figure 3.7) is designed for the standard-sample bracketing technique

in order to correct for the instrumental mass fractionation during the measurement (Aggarwal et al., 2003).

Several international reference materials were used to further QA/QC examination, including the boric acid international standard NIST 951, an in-house standard Alfa-B (High purity boron standard solution, Alfa Aesar, calibrated by NCKU), IAEA-B1 (seawater standard) and JCp-1 (coral standard). Their $\delta^{11}B$ values were analyzed after the micro-sublimation, and the values obtained were 0.01±0.25‰ (2SD, n=105), -5.35±0.20‰ (2SD, n=55), +39.6±0.24‰ (2SD, n=25) and +24.25±0.24‰ (2SD, n=20), respectively. All these results are consistent with the recommended $\delta^{11}B$ values, illustrating the usefulness of the described approach.
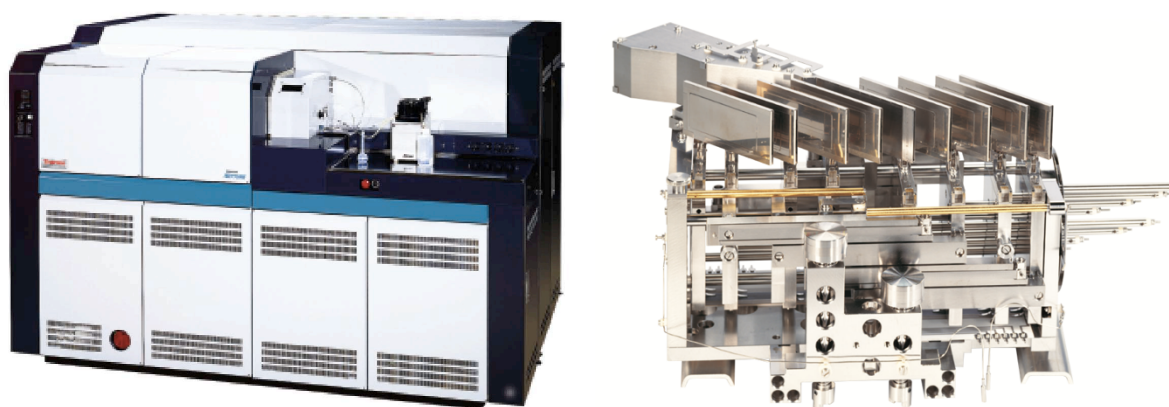
Figure 3.6   The high resolution multiple collector inductively coupled plasma mass spectrometer (NEPTUNE *Plus*, Thermo-Fisher Scientific[TM]) (a) Appearance (b) The detection system (Faraday cups).

Table 3.2 Operating conditions for MC-ICP-MS in this study.

parameters	Setting value
RF Power	1200 W
Fore Vaccum	$1.11 \times 10^{-3} \sim 1.52 \times 10^{-3}$ mbar
High Vaccum	$2.35 \times 10^{-7} \sim 3.06 \times 10^{-7}$ mbar
Ion Gatter Pressure	$4.71 \times 10^{-9} \sim 12.8 \times 10^{-9}$ mbar
Sampling Gas Flow rate	$1.000 \sim 1.050$ L/min
Cooling Gas Flow rate	16 L/min
Auxiliary Gas Flow rate	0.8 L/min
Nebulizer Type	PFA microflow 100μL/min
Peristaltic Pump Rate	15 rpm
Torch X-position	$-1.45 \sim 1.31$ mm
Torch Y-position	$-2.3 \sim 2.05$ mm
Torch Z-position	$-1.8 \sim 0.49$ mm
Focus	$-594 \sim -588$ V
X-Deflection	$-0.12 \sim 0$ V
Y-Deflection	$0 \sim 0.12$ V
Shape	$198 \sim 200$ V
Source Offset	-24 V
Focus Offset	50 V
Focus Quad	-2.8 V
Dispersion Quad	0 V

Blank (0.1N HNO₃)

↓

Standard (NIST 951)

↓

Sample 1

↓

Standard (NIST 951)

↓

Sample 2

↓

Standard (NIST 951)

↓

Blank (0.1N HNO₃)
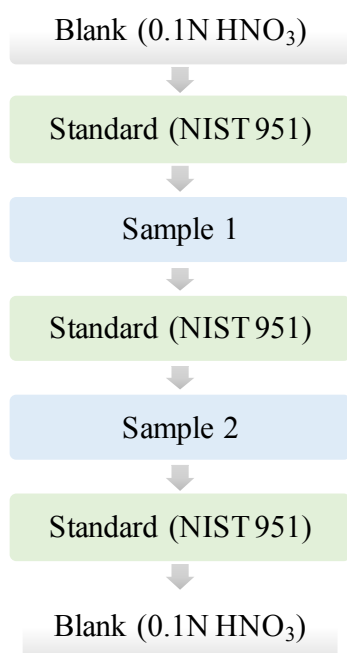
Figure 3.7 The analysis sequence flowchart for sample-standard bracketing approach (revealed in 2 samples as example)

CHAPTER 4   RESULTS AND DISCUSSION

4.1 Reconstruction of Sea Surface Temperature in the W-SCS

4.1.1 Foraminiferal Mg/Ca record over the last 22 kyr

The results of Mg/Ca ratio for *G. sacculifer* (without sac-like chamber, 425-500μm) from MD05-2901 are plotted with Mn/Ca, Al/Ca and Fe/Ca ratios (Fig 4.1) in order to feasibility of the cleaning step. No significant positive correlations between Mg/Ca and these three elemental ratios suggest that our Mg/Ca data are not subject to any contaminations from non-carbonate materials. Data are shown in Fig 4.2(a) and listed in Appendix S1. The Mg/Ca ratios display an increasing trend from the LGM to Holocene, ranging between 3.90 and 2.91 mmol/mol. Of special interest is that a clear decline was observed during the late HS1 and the maximum Mg/Ca value was found at 3.8 kyr, and then the Mg/Ca ratio drops ~0.32 mmol/mol at the late Holocene.
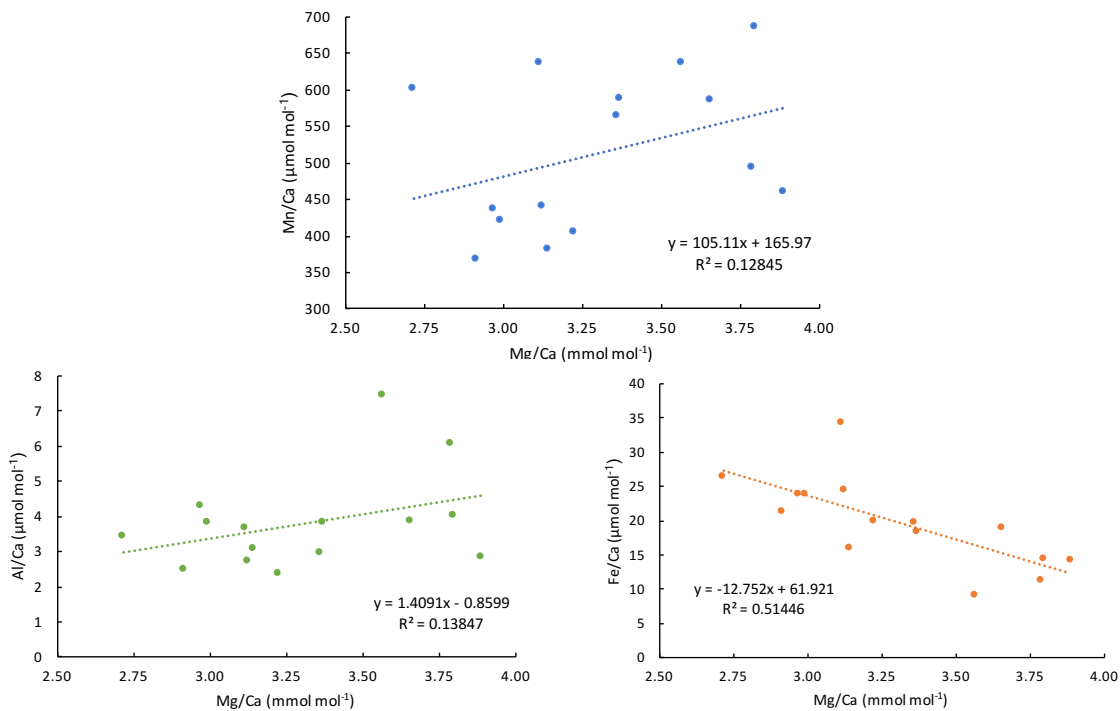
Figure 4.1   A comparison of Mg/Ca ratios with Mn/Ca, Al/Ca and Fe/Ca for the contamination examination in this study.

4.1.2 Mg/Ca thermometry for planktonic foraminifera *G.sacculifer*
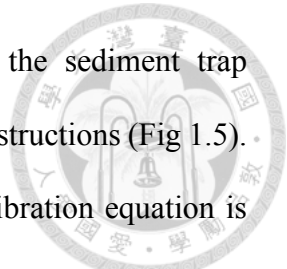
The Mg/Ca ratio in planktonic foraminifera shell is one of the most promising paleo-proxies for SST (see Section 1.3.2). Previous studies have shown the importance of the biological control on Mg incorporations for biogenic carbonates (e.g. Barker et al., 2005). In order to reconstruct the most reliable Mg/Ca-SST record, it is necessary to apply a suitable Mg/Ca-SST equation for the temperature reconstruction. Various attempts have been made to calibrate foraminiferal Mg/Ca ratios in *G. saccuifer* with SST, including culture (Nurnberg et al., 1996), core-top (Dekens et al., 2002; Rosenthal and Lohmann, 2002), and sediment trap approaches (Anand et al., 2003; Huang et al., 2008). However, there is no published Mg/Ca-SST equation for *G. sacculifer* with the size range of 425-500μm. We, therefore, estimated the SST in the W-SCS during the late Holocene and the LGM based on the existing Mg/Ca-SST equations. A comparison of the reconstructed SST for *G. sacculifer* at our study site is compiled in Table 4.1 and further discussed below.

Perhaps the most adequate Mg/Ca- SST calibration applied for SCS is from *in situ* empirical calibration from time series sediment trap in the northern SCS (Huang et al., 2008). The seasonal variations in SST and marine carbonate chemistry are observed in the SCS due to regional hydrological changes driven by East Asian Monsoon. Two dissolution-corrected Mg/Ca-SST equations are applied for the two seasons:

For fall-winter:
$$Mg/Ca = (0.38 - 0.02 * \text{water depth}) \cdot \exp(0.090 * T) \quad (4.1)$$

For spring-summer:
$$Mg/Ca = 0.30 \cdot \exp(0.090 * T) \quad (4.2)$$

Though the importance of *in situ* calibration and the seasonal variability are obvious in the SCS, this empirical calibration cannot be applied in this study due to the difference in size fraction (250-350 μm) as smaller *G. sacculifer* dwells in deeper part of the water column (Elderfield et al., 2002).

Mg/Ca-SST equation developed by Anand et al. (2003) using the sediment trap specimens in Sargasso Sea has been widely used for the paleo-SST reconstructions (Fig 1.5). For *G. sacculifer* without sac-like chamber (size 350–500 μm), the calibration equation is Mg/Ca = 1.06 · exp (0.048*T). However, they also indicated that all the planktonic foraminifera species should have a similar sensitivity for temperature.,The exponential component is, therefore, assumed to be a constant value of 0.090 for the planktonic species (Eq 4.3).

$$Mg/Ca \ = \ 0.347 \cdot exp\,(0.090 * T) \tag{4.3}$$

Another Mg/Ca- SST equation established by Dekens et al. (2002) using the core-top sediments is also widely applied for the temperature reconstructions. Considering both the core depth for the dissolution term and the sampled location, the Mg/Ca-SST equation for *G. sacculifer* in the Pacific Ocean is:

$$Mg/Ca = 0.37 \cdot exp\,0.090 * [T - 0.36(\text{core depth km}) - 2.0\text{°C}] \tag{4.4}$$

Because of the large difference in sample size selection and in the cleaning procedure between studies, the core-top SST (28.75℃) is different from modern value (27.5℃).

Wei et al. (2007) suggested that there is another Mg/Ca- SST reconstruction study in northern SCS based on *G. sacculifer* without size selection. The calibration equation is evaluated by calculating two SST: the topmost sample and temperature change from LGM to Holocene. According to the results, they infer that the calibration from Nurnberg et al., 2000 is the most suitable for their data (T = (log Mg/Ca –log 0.491)/0.033).

For our approach, we first made a correction for different cleaning methods, and then applied to the Mg/Ca-SST equations described above. The reconstructed SST values for the core-top and the LGM are shown in Table 4.1. For the core-top samples, the reconstructed

SSTs are 26.9°C, 27.7°C and 28.8°C, using the equations of Anand et al. (2003), Huang et al. (2008) and, Deken et al. (2002), respectively. The Mg/Ca-SST equations of Anand et al (2003) and Huang et al (2008) are consistent with the modern SST (27.5°C, NOAA) in our study site. Considering the size fraction used in these two studies, the Mg/Ca-SST equation from Anand et al. (2003) is chosen in this study.

Nevertheless, several field-based and culture studies have shown Mg/Ca to increase with salinity (Allen et al., 2016 and references therein). The sea surface salinity (SSS) reconstruction often estimates by removing the temperature effect from $\delta^{18}O_{foram}$ records. However, Hönisch et al. (2013) had point out the inappropriate of directly apply the $\delta^{18}O_{residual}$ and Mg/Ca for SSS approach. Even though the salinity may exert an impact on Mg/Ca for paleo-SST, the uncertainties can be reduced by single down-core reconstruction. Furthermore, the monsoonal hydrological cycle in SCS has exerted a major impact on the sea surface $\delta^{18}O$ compositions which could valid the paleo-SSS inherit from it (Wang et al., 2016). Hence, the salinity correction for $SST_{Mg/Ca}$ is not applied in this study.

45
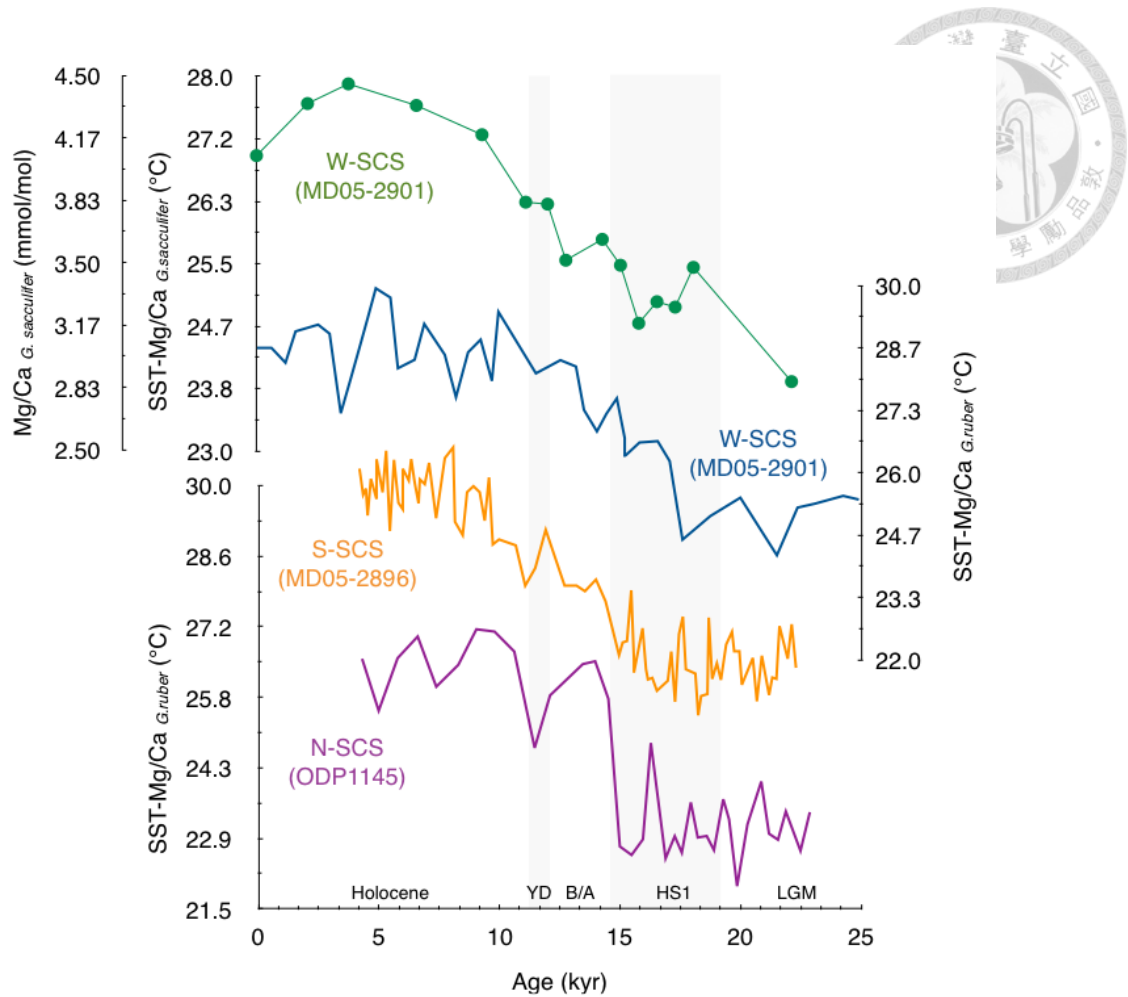
Figure 4.2　Sea surface temperature in South China Sea during 25kyr based on Mg/Ca ratios in planktonic foraminifera. (a) $SST_{Mg/Ca}$ record of *G. sacculifer* in western SCS (MD05-2901, this study), (b) $SST_{Mg/Ca}$ record of *G. ruber* in western SCS (MD05-2901, Wang et al., 2012), (c) $SST_{Mg/Ca}$ record of *G. ruber* in southern SCS (MD05-2896, Tian et al., 2010), (d) $SST_{Mg/Ca}$ record of *G. ruber* in northern SCS (ODP1145, Oppo and Sun, 2005).

Table 4.1   Comparison between published Mg/Ca- SST equations for *G. sacculifer*.

	Anand et al.,2003	Dekens et al., 2002	Huang et al., 2008
Source	Sediment trap	Core top	Sediment trap
	G. sacculifer w/o sac	*G. sacculifer* w/o sac	*G. sacculifer* w/o sac
Size	350-500 μm	250-350 μm	250-350 μm
Equation	Eq 4.3	Eq 4.4	Eq 4.1(for winter) Eq 4.2 (for summer)
Equation (Mg/Ca=B×exp(A·T))			
B	1.06	0.37	0.38 (for winter) 0.30 (for summer)
A	0.09 (Assumed)	0.09	0.09
Depth correction	-	V	V (for winter) - (for summer)
Region correction	-	V (Pacific)	-
Cleaning procedure comparison			
Reductive step	-	V	V
Reconstructed SST (Modern SST=27.5°C)			
Core-top	26.9℃	28.8℃	27.7℃[*]
22kyr	23.9℃	25.7℃	24.7℃[*]

(* is the average for winter and summer equations)
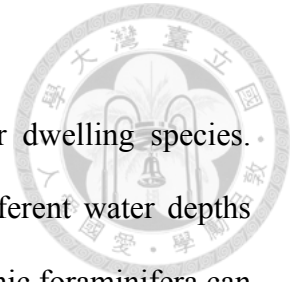
4.1.3 Inter-species Foraminiferal Mg/Ca

Previous studies had shown that *G. sacculifer* is a mixed-layer dwelling species. However, the different size fractions of *G. sacculifer* may live in different water depths (Elderfield et al., 2002). The calcification depth for the selected planktonic foraminifera can be estimated by a comparison between foraminiferal $\delta^{18}O_c$ and theoretically predicted $\delta^{18}O_c$ at various depths. For the SCS, the sediment trap data indicate that the calcification depth of *G. ruber* is 0-20 m and is 0-50 m for *G. sacculifer* (Huang et al., 2008), which is in agreement with the results based on the specimens collected by the plankton tow and the sediment trap (Lin et al., 2004).

In order to confirm that shell chemistry for the large size fraction (425-500μm) of *G. sacculifer* can represent the surface condition of W-SCS, the Mg/Ca records for *G. ruber* from the same core (Wang and Li, 2012) is used to further compare with our data. The deglacial SST variability reconstructed from *G. ruber* in the W-SCS ranged from ~24°C during the LGM to 27.7°C in the late Holocene (Fig 4.2(b)) (Wang and Li, 2012). This result is excellent agreement with our Mg/Ca-SST record based on the large size fraction of *G. sacculifer* (23.9°C for LGM and 27.5°C for late Holocene). As a result, the selected size fraction (425-500μm) for *G. sacculifer* can be considered as a reliable recorder for surface ocean condition.

4.1.4 Deglacial Sea Surface Temperature variability in the W-SCS

The reconstructed SST record in the W-SCS ranges from 27.5°C to 23.9°C during the last deglaciation (Fig 4.2(a)), and temperature difference between the late Holocene and the LGM is ~4°C. The SST gradually increased from the LGM to the mid-Holocene with two

48

cooling trends at the HS1 and the late Holocene (after ~5-6 kyr B.P.). The overall reconstructed SST pattern in the W-SCS is coherent with the deglacial warming.

4.1.5 Deglacial $SST_{Mg/Ca}$ variability in the SCS

In order to better understand the climate response in the SCS during the last deglaciation, a comparison of the reconstructed $SST_{Mg/Ca}$ records from the N-SCS (Oppo and Sun, 2005), the S-SCS (Tian et al., 2010) and the W-SCS (Wang and Li, 2012 and this study) is shown in Fig. 4.2. The SST in these three regions reached the highest temperature at the mid-Holocene, and were consistently lowered by ~4°C during the LGM. The SST in the SCS shows a strong latitudinal pattern: the average late Holocene SST is ~26°C, ~27.8°C, and ~28.5°C for the N-, W- and S-SCS, respectively. For the LGM, the average SST is ~22°C, ~25°C, and ~25.2°C for the N-SCS, W-SCS and S-SCS, respectively. The southern part of the SCS is always warmer than the other regions in the SCS throughout the last deglaciation.

In the earlier work, the reconstructed $SST_{Mg/Ca}$ in the W-SCS during the MIS 5 is ~ 2°C lower than the N-SCS (Wang and Li, 2012), and they attributed this difference to the influence of strong summer upwelling in the W-SCS during the interglacial time. However, there is no clear evidence for the dominant influence of summer monsoon on the SST during the last deglaciation based on the data we generated. Instead, our results suggested that the latitudinal control is the predominant factor for the SST distribution in the SCS.

The deglacial SST variability in the SCS may provide valuable information on how the ocean gets warmed since the LGM. In tropical/subtropical Pacific and Sulu Sea, the deglacial SST trends show a gradual increase since the LGM without any of these abrupt climate oscillations (continuous deglacial warming patterns) (e.g. Koutavas and Joanides, 2012; Rosenthal et al., 2003). However, the $SST_{Mg/Ca}$ results both in W-SCS from this study and

49

other SCS areas illustrated that abrupt climate events, such as HS1, B/A, YD, are recorded during the deglacial warming (Fig 4.2). These SST patterns are classified as the marginal sea type by Kiefer and Kienast (2005). The strong coupling of deglacial SST in SCS and climate events of the North Atlantic (e.g. iceberg melting and meridional overturning circulation variation) rather than tropical/subtropical Pacific suggests that marginal seas are significantly influenced by continental/atmospheric variability than open ocean. In order to better constrain the hydrologic variability in the SCS rather responses to the global climate change or the EAM during the last deglaciation, the further numerous high-resolution $SST_{Mg/Ca}$ records are still required.

50
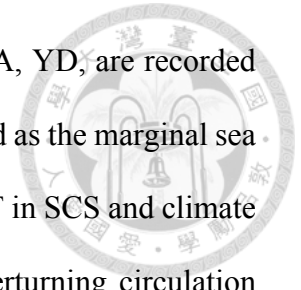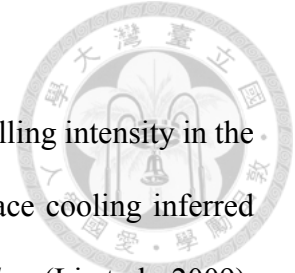
4.2 Reconstruction of EASM-driven upwelling intensity

Previous studies had attempted to reconstruct past changes in upwelling intensity in the W-SCS using a variety of geochemical approaches. For instance, surface cooling inferred from planktonic foraminifer fauna (Yu et al., 2008), $U^{K'}_{37}$-SST of *G.ruber* (Li et al., 2009), and Mg/Ca-SST of *G.ruber* (Wang et al., 2012) were linked to enhanced upwelling intensity during 135ka. On the other hand, geochemical proxies for primary productivity were also applied in the SCS sediments, including the Cd/Ca ratios in *N. dutertrei* (Lin et al., 1999), accumulation rates of total organic carbon and alkenones (Heilig, 1996). All these approaches illustrated a connection between upwelling water and monsoon intensity over geological time scale. The stronger upwelling in W-SCS consisted with EASM would occur in the interglacial/warm events, while both weaken in glacial/cold events. Above approaches have their strength and drawback, therefore, a multi-proxy approach is required to better constrain the past upwelling intensity in the SCS during the last deglaciation. In this study, we first access the utility of the Ba/Ca ratio in *G. sacculifer*, as a reliable proxy for upwelling intensity, and then present a new foraminiferal Ba/Ca record from the W-SCS.

4.2.1 Foraminiferal Ba/Ca ratio as a proxy for past upwelling intensity

The Ba/Ca ratio of planktonic foraminifer shells can faithfully record the Ba concentration in seawater, and is independent of other parameters such as temperature, salinity, and pH (Hönisch et al., 2011 and references therein). Thus, foraminiferal B/Ca may be a promising proxy for upwelling intensity in association with primary productivity (e.g. Lea and Boyle, 1991), or an indicator of sea surface salinity, which is related to river water discharge in coastal areas and estuaries (e.g. Bahr et al., 2013; Hall and Chan, 2004).

51

In the N-SCS, the dissolved concentration of Ba ([Ba]) in the surface ocean is 40.2 nmol kg^{-1} and δ^{137}Ba is 0.9±0.1 ‰ (18.3°N, 115.7°E, water depth of 5.2 m, salinity = 33.88) (Fig 4.3) (Cao et al., 2016). The [Ba] increases with the depth for the upper 1500 m and possesses the nutrient-type distribution as a general feature in the SCS, where river input and deepwater upwelling are excluded. In our study area, the W-SCS, its hydrologic properties are affected by coastal upwelling during the summer (Fig 2.2). The upwelled water is characterized by not only cold and nutrient-rich, but also high in [Ba]. Accordingly, the surface water [Ba] should be higher in the upwelling region than other regions. On the basis of the modern observation, the upwelling in the W-SCS can be linked to East Asian Summer Monsoon due to Ekman transport. Another possible controlling factor for seawater [Ba] is the riverine input, but is neglected since our study site is distant from the land and no major rivers flow into this region. Mekong River, the largest river near the study site, does not have a strong influence on seawater chemistry in the W-SCS based on SSS observation data (Fig 4.4) (Wang et al., 2002). In other words, the upwelling intensity is most likely the main control on seawater [Ba] in the W-SCS.
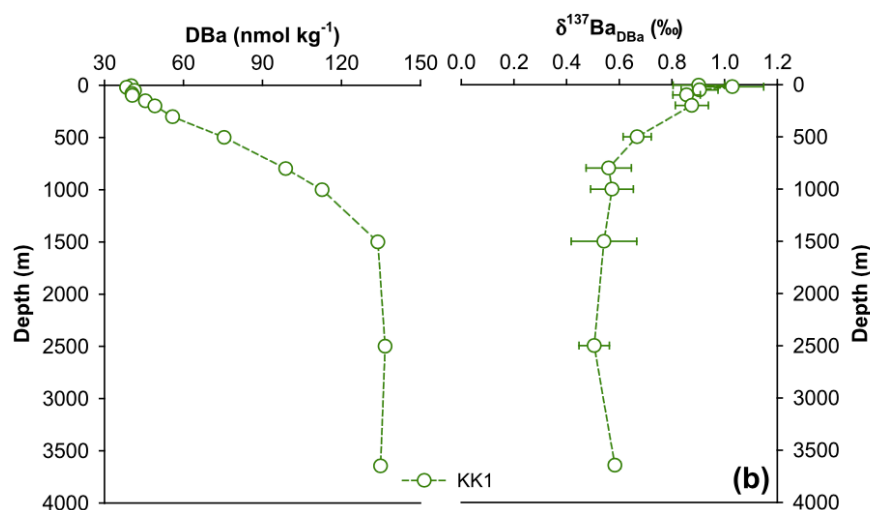
Figure 4.3 Vertical distributions of dissolved barium concentrations and its stable barium isotopic compositions in northern South China Sea (Cao et al., 2016).

52
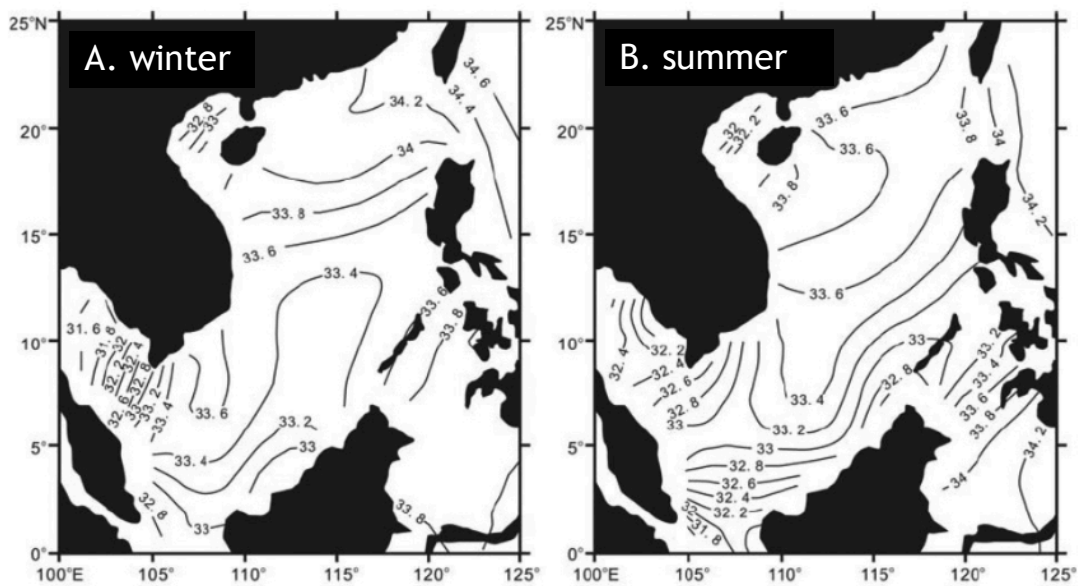
Figure 4.4 Sea surface salinity (‰) in the modern SCS show distinct seasonality patterns in (A) winter and in (B) summer (Wang et al., 2002). The SSS in W-SCS is mainly controlled by ocean water rather than terrestrial rivers.

4.2.2 Down-core Ba/Ca record in the W-SCS

The Ba/Ca data of *G. sacculifer* in core MD05-2901 are first compared to the existing Ba/Ca record (*G. ruber*) from core MD03-2707, which is located in the Gulf of Guinea, West Africa (Weldeab et al., 2007). The foraminiferal Ba/Ca ratio with the value exceeding 3 μmol mol^{-1} is not shown due to potential influences of post-depositional alteration or barites (Lea and Boyle, 1991; Weldeab et al., 2007). As the largest marginal sea in the western Pacific, the SCS receives tremendous amounts of continental materials, and thus, the SCS sediments are much dirtier than the sediments collected in the open ocean. The cleaning procedure using DTPA solution is, therefore, needed for removing barites in the SCS sediments (Lea and Boyle, 1991). To further evaluate the feasibility of the cleaning step, the Ba/Ca ratios are plotted with Mn/Ca, Al/Ca and Fe/Ca ratios (Fig 4.5). No significant correlation between

Ba/Ca and Mn/Ca is observed, indicating that our down-core Ba/Ca records should reflect largely the seawater [Ba].

The Ba/Ca ratios of *G. sacculifer* in core MD05-2901 range from 1.14 to 2.30 µmol mol^{-1} over the past 22 kyr (3.8-22ka, Fig 4.6(c)). During the LGM and HS1, the foraminiferal Ba/Ca ratios were low, and then rapidly increased during the B/A warm interval. Between the B/A and the YD, the Ba/Ca ratios gradually declined, and then remained stable throughout the late Holocene.
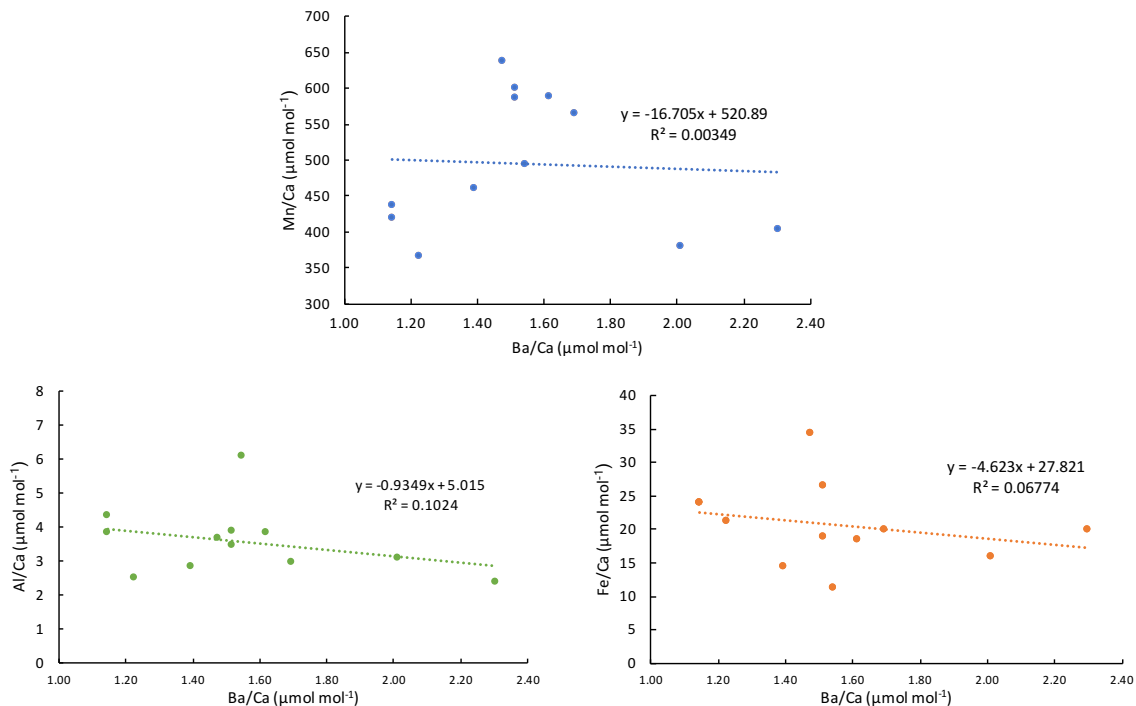
Figure 4.5 Comparison Ba/Ca ratios with Mn/Ca, Al/Ca and Fe/Ca for the contamination examination in this study.
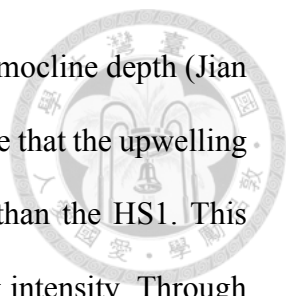
4.2.3 Upwelling intensity in the W-SCS during the last deglaciation

Based on the foraminiferal Ba/Ca record, the changes in upwelling intensity in the W-SCS is reconstructed over the last 22 kyr (Fig 4.6(c)). As the higher Ba/Ca ratios correspond to stronger upwelling intensity, our record demonstrates that the upwelling intensity reached the maximum condition at the B/A, and relatively weak during HS1 and the YD cold events. If the upwelling intensity is the main control for seawater [Ba] in the W-SCS, our results suggest that the upwelling intensity is more vigorous at interstadials than stadials. After the YD, the reconstructed upwelling intensity did not significantly change throughout the late Holocene. In order to validate the Ba/Ca ratios in *G. sacculifer* as a proxy for past upwelling intensity in the W-SCS, we further compared our Ba/Ca record to the published results for past changes in upwelling intensity in the W-SCS.

(1) Ba/Ca record for past upwelling intensity in the W-SCS

In the modern W-SCS, increasing upwelling intensity driven by East Asia Summer Monsoon results in high primary productivity in the surface ocean (Fig 2.2). Core SO17954 in the W-SCS had been studied for reconstructing past changes in primary productivity based on the accumulation rates of total organic carbon and alkenones (Fig 4.6(d-g), Heilig, 1996), planktc $\delta^{13}C$ (Wang et al., 1999), brassicasterol component (Li et al., 2015a). All these records vary synchronously with our foraminiferal Ba/Ca data, suggesting that foraminiferal Ba/Ca ratios may directly response to primary productivity in the surface ocean, and are associated with upwelling intensity in the W-SCS.

Another approach for constraining past changes in upwelling intensity is to reconstruct the thermocline depth in the past. Strong upwelling intensity would shoal the depth of thermocline (DOT), and thus reduced the temperature difference between subsurface and surface ocean. Previous studies had combined planktonic foraminifera

fauna assemblages and used transfer functions to reconstruct the thermocline depth (Jian et al., 2001; Yu et al., 2008; Yu et al., 2006). Their results demonstrate that the upwelling intensity of the W-SCS is stronger during the B/A warm interval than the HS1. This highlights the important role of EASM for influencing the upwelling intensity. Through the Ekman transport, the W-SCS coastal upwelling is driven by EASM winds. Therefore, these proxies, including the foraminiferal Ba/Ca ratios, paleoproductivity and DOT, are indicative of deglacial EASM variability. In general, EASM is stronger during the B/A warm period and weaker at the cold intervals such as the YD, HS1 (Fig 4.6(c-g)).

(2) Deglacial EASM variability reconstructed from speleothem records

In addition to the marine records, the Chinese speleothem $\delta^{18}O$ records provide an alternative approach for the reconstruction of EASM intensity (Fig 4.6(h-i), Dykoski et al. (2005); Wang et al. (2001). Variations in insolation and global ice volume are the main factors that control climate changes since the late Pleistocene. The enhanced EASM can be linked to the strongest Northern Hemisphere summer insolation (Fig 4.6(j)). The speleothem $\delta^{18}O$ records can be used to reconstruct the precipitation driven by EASM. The lower $\delta^{18}O$ data in interstadials indicates stronger EASM, which co-varies with the marine records. However, there is a discrepancy between marine and terrestrial records in Holocene. For instance, the speleothem $\delta^{18}O$ records show that enhanced EASM does not appear in marine records after the YD. This inconsistence needs to be further evaluated in the future work. In summary, the Ba/Ca ratio in *G. sacculifer* can serve as a proxy for past upwelling intensity in the W-SCS. The coastal upwelling off Vietnam was controlled by EASM during the last deglaciation.

56
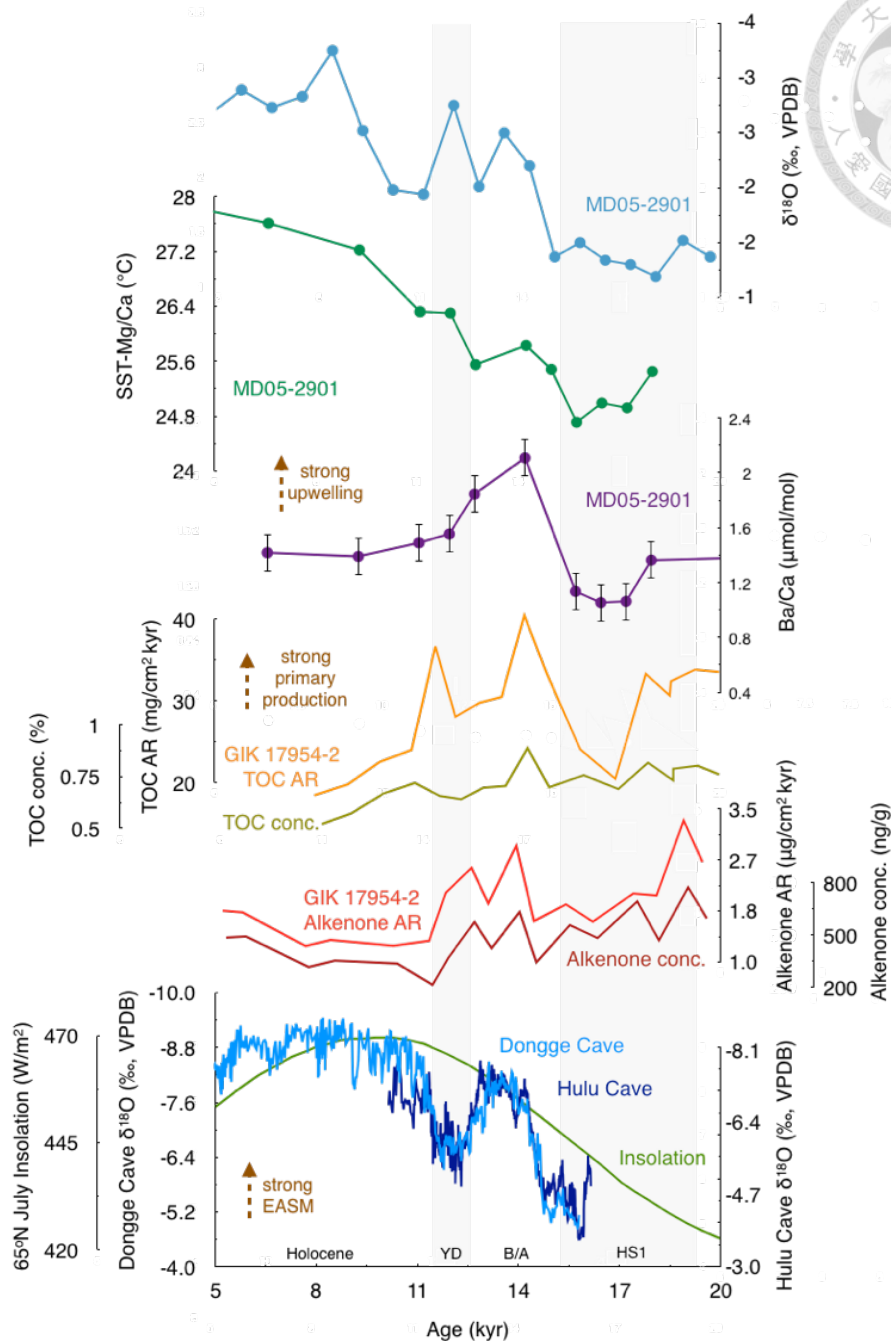
Figure 4.6 Comparison between the Ba/Ca- upwelling intensity record from core MD05-2901 and other summer monsoon indicators during last 5-20 kyr. (a) $\delta^{18}O$ record of *G. ruber* in core MD05-2901 (Li, 2007); (b) $SST_{Mg/Ca}$ record of *G. sacculifer* in core MD05-2901 (this study); (c) Ba/Ca record of *G. sacculifer* in core MD05-2901(this study); (d-g) Concentrations and accumulation rates (AR) of total organic carbon (TOC, yellow line) and alkenones (red line) in core 17954 (Heilig, 1996); (h) Speleothem $\delta^{18}O$ record in Dongge Cave (Dykoski et al.,2005); (i) Speleothem $\delta^{18}O$ record in Hulu Cave (Wang et al.,2001); (j) Summer insolation during July at 65°N (Berger and Loutre, 1991).

57
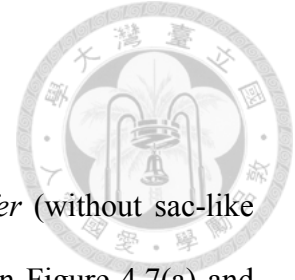
4.3 Reconstruction of surface ocean pH in the W-SCS

4.3.1 Foraminiferal δ^{11}B record in MD05-2901

The δ^{11}B record for the surface-dwelling foraminifer *G. sacculifer* (without sac-like chamber, 425-500μm) in the W-SCS core MD05-2901 were showed in Figure 4.7(a) and listed in Appendix Table S2. Foraminiferal δ^{11}B values vary from +20.07‰ to +18.68‰, and display a change of ~ 2‰ (~0.2 pH units) between the LGM and the Holocene epoch. There are two positive excursions in our δ^{11}B record. The first excursion started at 22kyr and the δ^{11}B values increase ~1.5‰; the second one started from 12kyr and the δ^{11}B values increase ~1.8‰. This indicates that the δ^{11}B values are low during the LGM and cold intervals, such as HS1 and YD, and then gradually increase towards to the warm periods. The δ^{11}B record during the warm periods, the B/A and late Holocene, does not exhibit a large fluctuation, but features relatively high δ^{11}B values compared to the cold periods.

4.3.2 Validation of boron isotope pH proxy for *G. sacculifer*

The boron isotopic compositions of foraminiferal shells have been widely used as a reliable proxy for past oceanic pH. The incorporation of boron not only follows the thermodynamics but also species-specific physiological processes in foraminifera (see Section 1.3). In this study, the measured δ^{11}B values of *G. sacculifer* are converted to seawater pH using the equations established by Foster et al. (2012) and Henehan et al. (2016).

In order to further validate the relationship between δ^{11}B in calcium carbonates and ambient water pH, recent studies have compiled the reported data from both inorganic precipitation experiments (Sanyal et al., 2001, N-TIMS) and core-top specimens (Foster, 2008; Martínez-Botí et al., 2015, MC-ICP-MS). Though the interlaboratory calibration, an offset of -3.32‰ is applied when using the δ^{11}B data measured by N-TIMS (Foster et al.,

2013). With this correction, the relationship between δ^{11}B in *G. sacculifer* and ambient water pH can be further defined by using a larger dataset from published results (Martínez-Botí et al., 2015). Since the size effect on δ^{11}B of *G. sacculifer* is significant (see Section 3.1.3), data comparison is only done for those of test size > 425 μm. The equation for calculating the δ^{11}B$_{borate}$ from δ^{11}B$_{calcite}$ for *G. sacculifer* (>425 μm) is listed below (equation from Henehan et al., 2016, with 2σ uncertainties):

$$\delta^{11}B_{borate} = (\delta^{11}B_{calcite} - 3.94 \pm 4.02) / 0.82 \pm 4.02 \qquad (4.5)$$

The seawater pH value can be calculated by δ^{11}B of *G. sacculifer* through the following equation:

$$pH = pK_B^* - \log(-\frac{\delta^{11}B_{SW} - \delta^{11}B_{CaCO_3}}{\delta^{11}B_{SW} - \alpha_B \delta^{11}B_{CaCO_3} - 1000(\alpha_B - 1)}) \qquad (1.16)$$

The dissociation constant for boric acid (pK$_B$*) is assumed to be 8.597 at 25°C, 35 psu,1 atm (Dickson, 1990), the boron isotopic composition of seawater (δ^{11}B$_{SW}$) is 39.61‰ (Foster et al., 2010), and the isotopic fractionation between the two aqueous species of boron in seawater ($^{11-10}$K$_B$) is 1.0272±0.0006 (Klochko et al., 2006). With the above information, the reconstructed pH value for the SCS core-top sample (SO 17940) is 8.16, in agreement with the modern seawater pH (pH = 8.2, Chen et al., 2006) near our study site.

4.3.3 Deglacial variability in δ^{11}B-derived pH in the W-SCS

δ^{11}B-derived seawater pH varied from 8.05 to 8.20 in the W-SCS over the last 22 kyr (Fig 4.7). During the warm periods, the average seawater pH value is 8.13 for the late Holocene and 8.17 for the B/A event. For the cold periods, average surface pH values for the YD, early HS1 and the LGM is 8.06, 8.10 and 8.14, respectively. As mentioned in Section 4.3.1, deglacial variability in seawater pH of the W-SCS was characterized by two gradual

increases: the first one increased by 0.08 pH units from 22 kyr to 12.8kyr, and second one increase by 0.11 pH units from 12 kyr to the present. In contrast, a very small difference (~0.02 pH units) in surface pH between the LGM (one data point) and the late Holocene in the W-SCS. Apparently, this is not consistent with the reconstructed seawater pH records from other cores during the last deglaciation. For example, ~0.18 pH units for the east Pacific upwelling region (Martínez-Botí et al., 2015), ~0.08 pH units for the western equatorial Pacific (Palmer and Pearson, 2003), ~0.09 pH units for the Caribbean Sea (Foster, 2008) and ~0.14 pH units for the eastern equatorial Atlantic (Hönisch et al., 2009). A more detailed investigation on the seawater pH during the LGM is needed in order to further our understanding about the relationship between global carbon cycle and hydrologic condition during the last deglaciation.
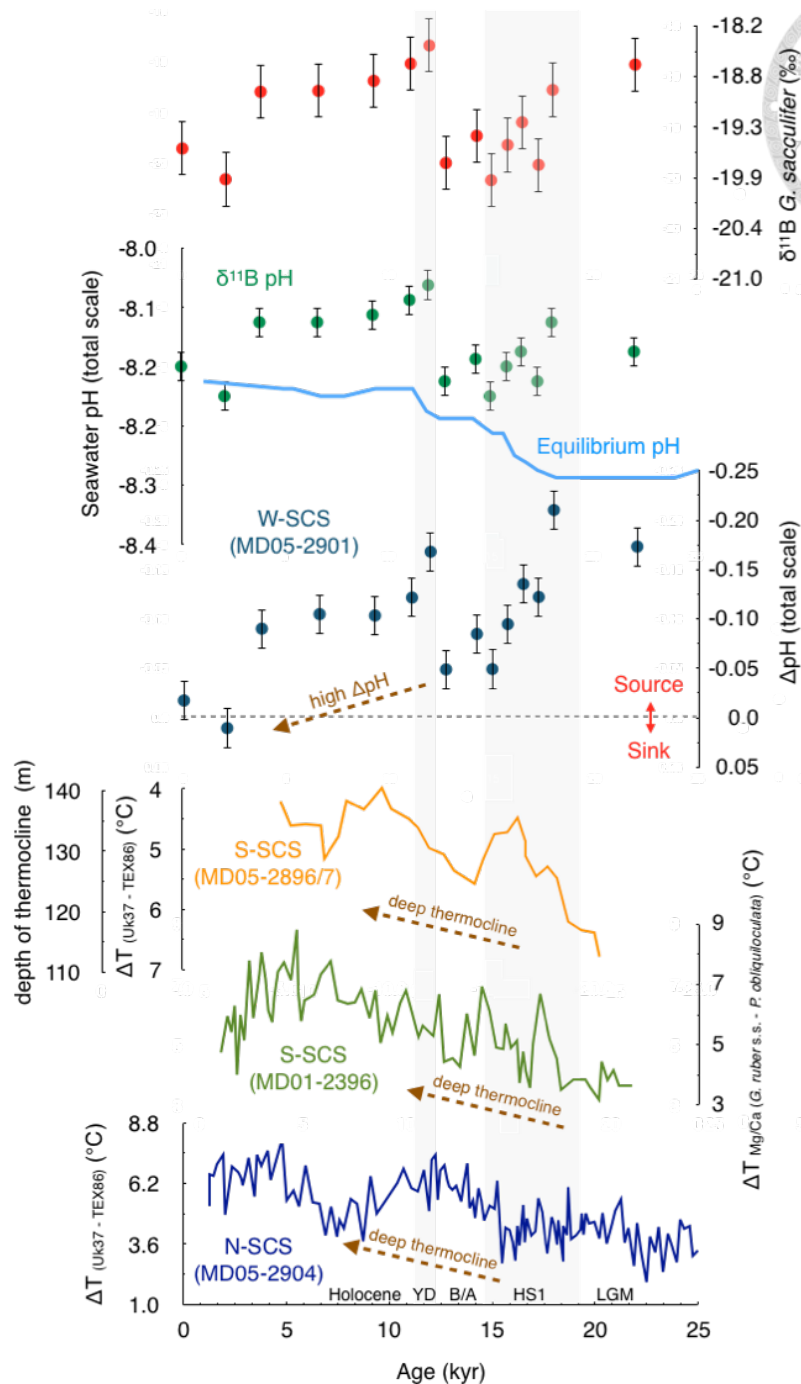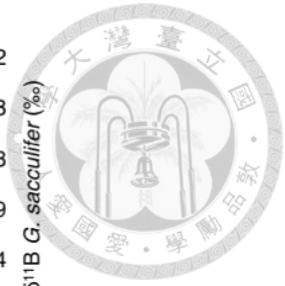
Figure 4.7 Reconstructed surface pH in western South China Sea during 25kyr based on $\delta^{11}B$ of planktonic foraminifera. (a) $\delta^{11}B$ of *G. sacculifer* in this study; (b) $\delta^{11}B$-based pH and calculated seawater pH in equilibrium with $p\mathrm{CO}_{2atm}$; (c) pH difference between surface ocean and equilibrium pH; (d) Depth of thermocline record in S-SCS derived from the difference between $U^{37'}_{K}$–SST and TEX^{H}_{86}-SSST (Dong et al.,2015); (e) Depth of thermocline record in S-SCS derived from the difference between $SST_{Mg/Ca(G.ruber)}$ and $SSST_{Mg/Ca(P.obliquiloculata)}$ (Steinke et al.,2010); (f) Depth of thermocline record in N-SCS derived from the difference between $U^{37'}_{K}$–SST and TEX^{H}_{86}-SSST (Steinke et al.,2011).

61

4.3.4 CO_2 outgassing in the W-SCS during the last deglaciation

To better understand the evolution of the marine carbonate system during the last deglaciation, the determination of ocean-atmosphere CO_2 exchange is required. Reconstruction of partial pressure of CO_2 in seawater ($pCO_{2\text{-}SW}$) is excluded, as it is difficult to constrain another parameter of the marine carbonate system in this study (see Section 1.3.3). We therefore applied the pH difference ($\Delta pH_{(sea\text{-}air)}$) between surface ocean and the pH value that is in equilibrium with the contemporary atmospheric CO_2 derived from the ice core record (Schmitt et al., 2012) in order to determine the ocean-atmosphere CO_2 exchange. When $\Delta pH_{(sea\text{-}air)} < 0$, the surface water is more acidic than equilibrium pH, and surface ocean is defined as a CO_2 source to atmosphere. In contrast, $\Delta pH_{(sea\text{-}air)} > 0$ indicates that atmosphere is a CO_2 compared to the ocean. $\Delta pH_{(sea\text{-}air)}$ can be used as an indicator of a CO_2 source or sink for the surface ocean of the W-SCS.

The $\Delta pH_{(sea\text{-}air)}$ ranges from -0.21 to 0.02 pH units, and all the values are negative except for the late Holocene (Fig 4.7(d)), indicating that the W-SCS has been a constant source of CO_2 to the atmosphere throughout the entire time period covered by this study. Our $\Delta pH_{(sea\text{-}air)}$ record suggests that large amounts of CO_2 outgassed from the W-SCS at the beginning of HS1, followed by a gradual decrease (a weak source) in $\Delta pH_{(sea\text{-}air)}$ till the warm B/A. The W-SCS became a CO_2 source again during the YD and the $\Delta pH_{(sea\text{-}air)}$ gradually decreased to nearly zero during the late Holocene.

4.3.5 Possible mechanisms for deglacial seawater pH variability in the W-SCS

Based on the multi-proxy approach in this study, mechanisms that control the past changes in seawater pH include: (1) CO_2 solubility in the surface ocean, (2) Monsoon-driven upwelling, (3) Deep water circulation and (4) Depth of thermocline.
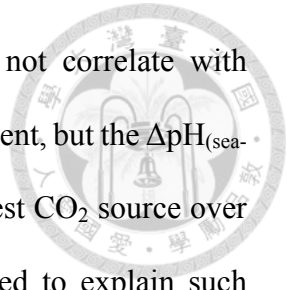
(1) CO_2 solubility in the surface ocean

In the surface ocean, two parameters, temperature and salinity, control the solubility of CO_2. Surface ocean would contain higher aqueous CO_2 at colder and saltier conditions, and vice versa. However, the modern observation shows that there is no clear relevance between the SST and pCO_{2sea} in the W-SCS (Zhai et al., 2013). In addition, the anticipated $\Delta pH_{(sea-air)}$ would be low in Northern Hemisphere cold intervals and high in warm events. This is obviously inconsistent with the reconstructed $\Delta pH_{(sea-air)}$ record.

Although the past changes in sea surface salinity (SSS) cannot be simply reconstructed by our study, previous studies have used paired measurements on foraminiferal $\delta^{18}O$ and Mg/Ca-SST (or other paleo-thermometer, such as U_K^{37}) for the SSS reconstruction (i.e. $\delta^{18}O_{residual}$) in SCS and adjacent areas (Oppo et al., 2003; Tian et al., 2006; Wang et al., 1999). Yet, Wang et al. (2016) argued that the $\delta^{18}O_{residual}$ might be not a reliable proxy for SSS in the SCS as the hydrology and oceanography in the SCS are modulated by East Asian Monsoon. Hence, whether SSS will affect the interpretation on deglacial seawater pH variability requires further evaluationsv.

(2) Monsoon-driven upwelling

The hydrological cycle in the surface W-SCS is largely driven by EASM upwelling (Xie et al., 2003). The nutrient- and CO_2-rich upwelling water results in a decrease in $\Delta pH_{(sea-air)}$ when mixing with surface water. During the last deglaciation, the upwelling
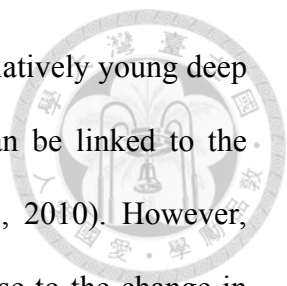
intensity reconstructed by our foraminiferal Ba/Ca record does not correlate with $\Delta pH_{(sea\text{-}air)}$. A strong upwelling signal is recorded at the B/A warm event, but the $\Delta pH_{(sea\text{-}air)}$ value does not coherently decrease and is even one of the weakest CO_2 source over the last 22 kyr. Accordingly, an alternative mechanism is required to explain such observation.

Another possible process that can influence the dissolved CO_2 concentration in the surface ocean is through the biological pump (Archer, 1995). This give a hypothesis that summer upwelling raises the nutrient levels in the surface W-SCS, which may enhance the biological pump and then possible reduces surface ocean pCO_2. A study at the upwelling region of the W-SCS shows that on top of upwelled DIC, microbial activities can play an important role for regulating the surface water pCO_2 (Jiao et al., 2014). These microbial activities stimulated by upwelled nutrients, along with labile organic carbon produced by phytoplankton, would increase the POC export flux. In addition, Ma et al. (2014) and Dai et al. (2013) both indicated that surplus DIC from deep ocean exerted a major impact on surface pCO_2 over SCS (see Section 2.2). However, the paleo-productivity proxy, such as TOC, might indicate the variation of biological process is consisted with EASM-influenced upwelling rather than surface pH (Fig 4.7). Nevertheless, whether biological process is an important component of carbon budget over geological time scale requires further paleo-biogeochemistry study.

(3) Deep water circulation

Mixing with different deep-water masses can also change the surface water pCO_2 concentrations in the W-SCS. During the last deglaciation, changes in deep-water circulation in the SCS are reported (e.g. Zhang et al., 2016). Data from the sedimentary magnetic properties suggest that a significant strengthening of the northeastward current

at the entrance of the SCS during HS1 (Zheng et al., 2016). This relatively young deep water is also found in the N-SCS (Wan and Jian, 2014), and can be linked to the formation of North Pacific Deep Water (NPDW, Okazaki et al., 2010). However, surface water pH reconstructed from our δ^{11}B data did not response to the change in Pacific deep-water circulation since the LGM, suggesting that deglacial variability in Pacific deep-water circulation may be not the main control on the surface water pH record in the W-SCS. Furthermore, foraminifera-based neodymium isotopic record in the N-SCS suggests increased flow of southern-sourced CO_2-rich water into the SCS during late HS1 (Wu et al., 2015). This is inconsistent with our δ^{11}B-derived pH record during this period.

(4) Depth of thermocline

The depth of thermocline (DOT) in the W-SCS is mainly driven by the regional wind stress. Stronger winds cause upwelling, and subsequently shoal the DOT. Therefore, a shoaling of the DOT results in a decline of surface water pH through mixing with CO_2-rich subsurface water. For the paleoceanographic studies, the past DOT variability in the SCS can be inferred by the difference between SST and subsurface seawater Temperature (SSST), based on mixed-layer and thermocline dwelling species of planktonic foraminifera, as well as organic geochemical proxies, such as $U^{37'}_K$ and TEX^H_{86} (Dong et al., 2015).

Previous studies show that the entire SCS shares a similar DOT variability during the last deglaciation, characterized by a gradual deepening of the DOT since the LGM (Fig 4.7(d-f)) (Dong et al., 2015; Steinke et al., 2011; Steinke et al., 2010). The deepening of the DOT further implies that the W-SCS should become less acidic through time, consistent with the deglacial surface water pH variability inferred from

65

$\delta^{11}B$ data in this study over the last 22 kyr. Hence, the high coherence between our $\Delta pH_{(sea-air)}$ record and $\Delta T_{SSS-SSST}$ from the SCS suggests that the DOT variation is most likely the controlling mechanism for the surface water pH in the W-SCS.

Nevertheless, this statement requires a further investigation on the DOT reconstruction in the W-SCS. Through the high-resolution reconstruction of the DOT variation in the W-SCS, along with reliable records of surface oceanic pH and upwelling intensity (see Section 4.2.3), we should be able to further our understandings of how carbon cycle in the SCS responses to the EAM system, and the playing role of the marginal seas for regulating the atmospheric CO_2 variation through time

CHAPTER 5   CONCLUSIONS
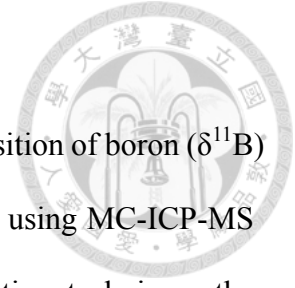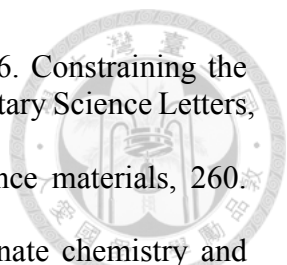
(1) A newly developed methodology for measuring the isotopic composition of boron ($\delta^{11}B$) and trace element ratios (TEs) in foraminifera (small size < 2 mg) using MC-ICP-MS and HR-ICP-MS is established. By applying the micro-sublimation technique, the external precisions for $\delta^{11}B$ and TEs (e.g., Mg/Ca, B/Ca, Li/Ca, Ba/Ca and U/Ca) determinations are better than ± 0.30 ‰ (2SD) and ± 2.0 %, (2SD), respectively.

(2) The Mg/Ca ratio of foraminiferal shell in the W-SCS displays an increasing trend from the LGM to Holocene, ranging between 3.90 and 2.91 mmol/mol. The reconstructed Mg/Ca-SST record suggests that the late Holocene SST was ~3°C higher than the glacial period, and reached the maximum value at around 3.8 kyr. During the late deglaciation, the SST in SCS is controlled by latitudinal. In addition, the large size fraction (425-500 μm) for *G. sacculifer* can be considered as a reliable recorder for surface ocean condition.

(3) The Ba/Ca ratio of *G. sacculifer* in the W-SCS is established as a proxy for past upwelling intensity. The Ba/Ca results range from 1.14 to 2.30 μmol mol^{-1} over the past 22 kyr. The wind-driven upwelling co-varied with EASM during the last deglaciation, which was stronger during the B/A warm period and weaker at the cold intervals, such as the YD and HS1. However, the discrepancy between marine and terrestrial records in the late Holocene still needs to be further evaluated.

(4) The $\delta^{11}B$-derived seawater pH varied from 8.05 to 8.20 in the W-SCS during the last deglaciation (+20.07‰ to +18.68‰ for $\delta^{11}B$), while displaying a rather small variation

of ~0.2 pH units (~ 2‰ for $\delta^{11}B$) between the LGM and the Holocene epoch. The pH

difference between seawater and the equilibrated pH with atmosphere indicates that the

W-SCS had been a constant source of CO_2 relative to the atmosphere throughout the last

deglaciation. This is most likely due to the basin-wide vertical mixing within the entire

SCS basin.
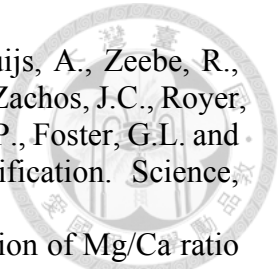
References
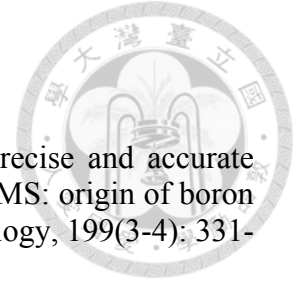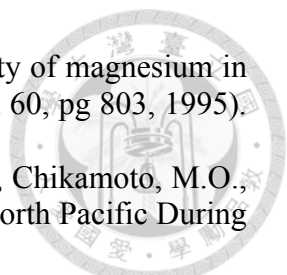
Aggarwal, J.K., Sheppard, D., Mezger, K. and Pernicka, E., 2003. Precise and accurate determination of boron isotope ratios by multiple collector ICP-MS: origin of boron in the Ngawha geothermal system, New Zealand. Chemical Geology, 199(3-4): 331-342.

Allen, K.A., Honisch, B., Eggins, S.M., Haynes, L.L., Rosenthal, Y. and Yu, J.M., 2016. Trace element proxies for surface ocean conditions: A synthesis of culture calibrations with planktic foraminifera. Geochimica Et Cosmochimica Acta, 193: 197-221.

Anand, P., Elderfield, H. and Conte, M.H., 2003. Calibration of Mg/Ca thermometry in planktonic foraminifera from a sediment trap time series. Paleoceanography, 18(2).

Archer, D., 1995. Upper Ocean Physics as Relevant to Ecosystem Dynamics - a Tutorial. Ecological Applications, 5(3): 724-739.

Bahr, A., Schonfeld, J., Hoffmann, J., Voigt, S., Aurahs, R., Kucera, M., Flogel, S., Jentzen, A. and Gerdes, A., 2013. Comparison of Ba/Ca and delta O-18(WATER) as freshwater proxies: A multi-species core-top study on planktonic foraminifera from the vicinity of the Orinoco River mouth. Earth and Planetary Science Letters, 383: 45-57.

Barker, S., Cacho, I., Benway, H. and Tachikawa, K., 2005. Planktonic foraminiferal Mg/Ca as a proxy for past oceanic temperatures: a methodological overview and data compilation for the Last Glacial Maximum. Quaternary Science Reviews, 24(7-9): 821-834.

Barker, S., Greaves, M. and Elderfield, H., 2003. A study of cleaning procedures used for foraminiferal Mg/Ca paleothermometry. Geochemistry Geophysics Geosystems, 4.

Bé, A.W.H., 1977. An ecological, zoogeographic and taxonomic review of recent planktonic foraminifera. Oceanic Micropaleontology, 1. Academic Press, London.

Bé, A.W.H., 1980. Gametogenic Calcification in a Spinose Planktonic Foraminifer, Globigerinoides-Sacculifer (Brady). Marine Micropaleontology, 5(3): 283-310.

Bentov, S., Brownlee, C. and Erez, J., 2009. The role of seawater endocytosis in the biomineralization process in calcareous foraminifera. Proceedings of the National Academy of Sciences of the United States of America, 106(51): 21500-21504.

Berger, A. and Loutre, M.-F., 1991. Insolation values for the climate of the last 10 million years. Quaternary Science Reviews, 10(4): 297-317.

Boyle, E.A., 1981. Cadmium, Zinc, Copper, and Barium in Foraminifera Tests. Earth and Planetary Science Letters, 53(1): 11-35.

Boyle, E.A. and Keigwin, L.D., 1985. Comparison of Atlantic and Pacific Paleochemical Records for the Last 215,000 Years - Changes in Deep Ocean Circulation and Chemical Inventories. Earth and Planetary Science Letters, 76(1-2): 135-150.

Broecker, W.S. and Peng, T.-H., 1982. Tracers in the Sea.

Cai, W.J., 2011. Estuarine and Coastal Ocean Carbon Paradox: CO2 Sinks or Sites of Terrestrial Carbon Incineration? Annual Review of Marine Science, Vol 3, 3: 123-145.

Cai, W.J., Dai, M.H. and Wang, Y.C., 2006. Air-sea exchange of carbon dioxide in ocean margins: A province-based synthesis. Geophysical Research Letters, 33(12).

Cao, Z.M., Siebert, C., Hathorne, E.C., Dai, M.H. and Frank, M., 2016. Constraining the oceanic barium cycle with stable barium isotopes. Earth and Planetary Science Letters, 434: 1-9.

Catanzaro, E.J., 1970. Boric acid: isotopic and assay standard reference materials, 260. National Bureau of Standards, Institute for Materials Research.

Chen, C.T.A., Wang, S.L., Chou, W.C. and Sheu, D.D., 2006. Carbonate chemistry and projected future changes in pH and CaCO3 saturation state of the South China Sea. Marine Chemistry, 101(3-4): 277-305.

Chou, W.C., Sheu, D.D., Lee, B.S., Tseng, C.M., Chen, C.T.A., Wang, S.L. and Wong, G.T.F., 2007. Depth distributions of alkalinity, TCO(2) and delta(13)C(TCO2) at SEATS time-series site in the northern South China Sea. Deep-Sea Research Part Ii-Topical Studies in Oceanography, 54(14-15): 1469-1485.

Cuffey, K.M. and Vimeux, F., 2001. Covariation of carbon dioxide and temperature from the Vostok ice core after deuterium-excess correction. Nature, 412(6846): 523-527.

Dai, M.H., Cao, Z.M., Guo, X.H., Zhai, W.D., Liu, Z.Y., Yin, Z.Q., Xu, Y.P., Gan, J.P., Hu, J.Y. and Du, C.J., 2013. Why are some marginal seas sources of atmospheric CO2? Geophysical Research Letters, 40(10): 2154-2158.

Dekens, P.S., Lea, D.W., Pak, D.K. and Spero, H.J., 2002. Core top calibration of Mg/Ca in tropical foraminifera: Refining paleotemperature estimation. Geochemistry Geophysics Geosystems, 3.

Dickson, A.G., 1990. Thermodynamics of the Dissociation of Boric-Acid in Synthetic Seawater from 273.15-K to 318.15-K. Deep-Sea Research Part a-Oceanographic Research Papers, 37(5): 755-766.

Dong, L., Li, L., Li, Q.Y., Wang, H. and Zhang, C.L.L., 2015. Hydroclimate implications of thermocline variability in the southern South China Sea over the past 180,000 yr. Quaternary Research, 83(2): 370-377.

Dykoski, C.A., Edwards, R.L., Cheng, H., Yuan, D.X., Cai, Y.J., Zhang, M.L., Lin, Y.S., Qing, J.M., An, Z.S. and Revenaugh, J., 2005. A high-resolution, absolute-dated Holocene and deglacial Asian monsoon record from Dongge Cave, China. Earth and Planetary Science Letters, 233(1-2): 71-86.

Elderfield, H. and Ganssen, G., 2000. Past temperature and delta O-18 of surface ocean waters inferred from foraminiferal Mg/Ca ratios. Nature, 405(6785): 442-445.

Elderfield, H., Vautravers, M. and Cooper, M., 2002. The relationship between shell size and Mg/Ca, Sr/Ca, delta O-18, and delta C-13 of species of planktonic foraminifera. Geochemistry Geophysics Geosystems, 3.

Foster, G.L., 2008. Seawater pH, PCO2 and [CO32-] variations in the Caribbean Sea over the last 130 kyr: A boron isotope and B/Ca study of planktic forminifera. Earth and Planetary Science Letters, 271(1-4): 254-266.

Foster, G.L., Honisch, B., Paris, G., Dwyer, G.S., Rae, J.W.B., Elliott, T., Gaillardet, J., Hemming, N.G., Louvat, P. and Vengosh, A., 2013. Interlaboratory comparison of boron isotope analyses of boric acid, seawater and marine CaCO3 by MC-ICPMS and NTIMS. Chemical Geology, 358: 1-14.

Foster, G.L., Lear, C.H. and Rae, J.W.B., 2012. The evolution of pCO(2), ice volume and climate during the middle Miocene. Earth and Planetary Science Letters, 341: 243-254.

Foster, G.L., Ni, Y.Y., Haley, B. and Elliott, T., 2006. Accurate and precise isotopic measurement of sub-nanogram sized samples of foraminiferal hosted boron by total evaporation NTIMS. Chemical Geology, 230(1-2): 161-174.

Foster, G.L., Pogge von Strandmann, P.A.E. and Rae, J.W.B., 2010. Boron and magnesium isotopic composition of seawater. Geochemistry Geophysics Geosystems, 11.

Foster, G.L. and Rae, J.W.B., 2016. Reconstructing Ocean pH with Boron Isotopes in Foraminifera. Annual Review of Earth and Planetary Sciences, Vol 44, 44: 207-237.

Gaillardet, J. and Allegre, C.J., 1995. Boron isotopic compositions of corals: Seawater or diagenesis record? Earth and Planetary Science Letters, 136(3-4): 665-676.

Gaillardet, J., Lemarchand, D., Gopel, C. and Manhes, G., 2001. Evaporation and sublimation of boric acid: Application for boron purification from organic rich solutions. Geostandards Newsletter-the Journal of Geostandards and Geoanalysis, 25(1): 67-75.

Hall, J.M. and Chan, L.H., 2004. Ba/Ca in Neogloboquadrina pachyderma as an indicator of deglacial meltwater discharge into the western Arctic Ocean. Paleoceanography, 19(1).

Heilig, S., 1996. Paläo-Ozeanographie vor Vietnam im Wandel von Glazial zu Interglazial. Unveröffentl, Diplomarbeit (Teil I: Laborarbeit), Mathematisch-Naturwissenschaftliche Fakultät der Christian-Albrechts-Universität zu Kiel.

Hemming, N.G. and Hanson, G.N., 1992. Boron Isotopic Composition and Concentration in Modern Marine Carbonates. Geochimica Et Cosmochimica Acta, 56(1): 537-543.

Henehan, M.J., Foster, G.L., Bostock, H.C., Greenop, R., Marshall, B.J. and Wilson, P.A., 2016. A new boron isotope-pH calibration for Orbulina universa, with implications for understanding and accounting for 'vital effects'. Earth and Planetary Science Letters, 454: 282-292.

Henehan, M.J., Rae, J.W.B., Foster, G.L., Erez, J., Prentice, K.C., Kucera, M., Bostock, H.C., Martinez-Boti, M.A., Milton, J.A., Wilson, P.A., Marshall, B.J. and Elliott, T., 2013. Calibration of the boron isotope proxy in the planktonic foraminifera Globigerinoides ruber for use in palaeo-CO2 reconstruction. Earth and Planetary Science Letters, 364: 111-122.

Hoecke, V.K., Devulder, V., Claeys, P., Degryse, P. and Vanhaecke, F., 2014. Comparison of microsublimation and ion exchange chromatography for boron isolation preceding its isotopic analysis via multi-collector ICP-MS. Journal of Analytical Atomic Spectrometry, 29(10): 1819-1826.

Hönisch, B., Allen, K.A., Lea, D.W., Spero, H.J., Eggins, S.M., Arbuszewski, J., deMenocal, P., Rosenthal, Y., Russell, A.D. and Elderfield, H., 2013. The influence of salinity on Mg/Ca in planktic foraminifers - Evidence from cultures, core-top sediments and complementary delta O-18. Geochimica Et Cosmochimica Acta, 121: 196-213.

Hönisch, B., Allen, K.A., Russell, A.D., Eggins, S.M., Bijma, J., Spero, H.J., Lea, D.W. and Yu, J.M., 2011. Planktic foraminifers as recorders of seawater Ba/Ca. Marine Micropaleontology, 79(1-2): 52-57.

Hönisch, B. and Hemming, N.G., 2004. Ground-truthing the boron isotope-paleo-pH proxy in planktonic foraminifera shells: Partial dissolution and shell size effects. Paleoceanography, 19(4).

Hönisch, B., Hemming, N.G., Archer, D., Siddall, M. and McManus, J.F., 2009. Atmospheric Carbon Dioxide Concentration Across the Mid-Pleistocene Transition. Science, 324(5934): 1551-1554.
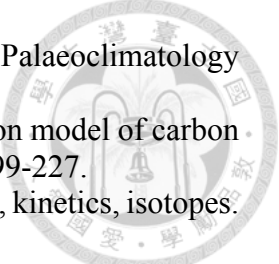
Hönisch, B., Ridgwell, A., Schmidt, D.N., Thomas, E., Gibbs, S.J., Sluijs, A., Zeebe, R., Kump, L., Martindale, R.C., Greene, S.E., Kiessling, W., Ries, J., Zachos, J.C., Royer, D.L., Barker, S., Marchitto, T.M., Moyer, R., Pelejero, C., Ziveri, P., Foster, G.L. and Williams, B., 2012. The Geological Record of Ocean Acidification. Science, 335(6072): 1058-1063.

Huang, K.F., You, C.F., Lin, H.L. and Shieh, Y.T., 2008. In situ calibration of Mg/Ca ratio in planktonic foraminiferal shell using time series sediment trap: A case study of intense dissolution artifact in the South China Sea. Geochemistry Geophysics Geosystems, 9.

IUPAC, 1998. Isotopic compositions of the elements 1997 (Technical Report). Pure and Applied Chemistry, 70(1): 217-235.

Jian, Z., Huang, B., Kuhnt, W. and Lin, H.L., 2001. Late quaternary upwelling intensity and east Asian monsoon forcing in the South China Sea. Quaternary Research, 55(3): 363-370.

Jiao, N., Zhang, Y., Zhou, K., Li, Q., Dai, M., Liu, J., Guo, J. and Huang, B., 2014. Revisiting the CO2 "source" problem in upwelling areas - a comparative study on eddy upwellings in the South China Sea. Biogeosciences, 11(9): 2465-2475.

Kakihana, H. and Kotaka, M., 1977. Equilibrium constants for boron isotope-exchange reactions. Bulletin of the Research Laboratory for Nuclear Reactors (Tokyo Institute of Technology), 2.

Kiefer, T. and Kienast, M., 2005. Patterns of deglacial warming in the Pacific Ocean: a review with emphasis on the time interval of Heinrich event 1. Quaternary Science Reviews, 24(7-9): 1063-1081.

Kiss, E., 1988. Ion-Exchange Separation and Spectrophotometric Determination of Boron in Geological-Materials. Analytica Chimica Acta, 211(1-2): 243-256.

Klochko, K., Kaufman, A.J., Yao, W.S., Byrne, R.H. and Tossell, J.A., 2006. Experimental measurement of boron isotope fractionation in seawater. Earth and Planetary Science Letters, 248(1-2): 276-285.

Koutavas, A. and Joanides, S., 2012. El Nino-Southern Oscillation extrema in the Holocene and Last Glacial Maximum. Paleoceanography, 27.

Laj, C., Wang, P. and Balut, Y., 2005. MD147-Marco Polo IMAGES XII Cruise Report. Brest: Institut Polaire Français.

Lea, D.W., 1999. Trace elements in foraminiferal calcite. Modern foraminifera: 259-277.

Lea, D.W. and Boyle, E.A., 1991. Barium in Planktonic-Foraminifera. Geochimica Et Cosmochimica Acta, 55(11): 3321-3331.

Lea, D.W., Mashiotta, T.A. and Spero, H.J., 1999. Controls on magnesium and strontium uptake in planktonic foraminifera determined by live culturing. Geochimica Et Cosmochimica Acta, 63(16): 2369-2379.

Lea, D.W. and Spero, H.J., 1994. Assessing the reliability of paleochemical tracers: Barium uptake in the shells of planktonic foraminifera. Paleoceanography, 9(3): 445-452.

Lee, K., Kim, T.W., Byrne, R.H., Millero, F.J., Feely, R.A. and Liu, Y.M., 2010. The universal ratio of boron to chlorinity for the North Pacific and North Atlantic oceans. Geochimica Et Cosmochimica Acta, 74(6): 1801-1811.

Lemarchand, D., Gaillardet, J., Gopel, C. and Manhes, G., 2002. An optimized procedure for boron separation and mass spectrometry analysis for river samples. Chemical Geology, 182(2-4): 323-334.

Li, J., 2007. Carbon reservoir in low-latitude oceans and orbital cycles of monsoon climate (in Chinese with English abstract)(Ph. D. thesis). Tongji University, China.

Li, L., Li, Q.Y., He, J., Wang, H., Ruan, Y.M. and Li, J.R., 2015a. Biomarker-derived phytoplankton community for summer monsoon reconstruction in the western South China Sea over the past 450 ka. Deep-Sea Research Part Ii-Topical Studies in Oceanography, 122: 118-130.

Li, L., Li, Q.Y., Li, J.R., Wang, H., Dong, L., Huang, Y.S. and Wang, P.X., 2015b. A hydroclimate regime shift around 270 ka in the western tropical Pacific inferred from a late Quaternary n-alkane chain-length record. Palaeogeography Palaeoclimatology Palaeoecology, 427: 79-88.

Li, L., Wang, H., Li, J., Zhao, M. and Wang, P., 2009. Changes in sea surface temperature in western South China Sea over the past 450 ka. Chinese science bulletin, 54(18): 3335-3343.

Libes, S., 2011. Introduction to marine biogeochemistry. Academic Press.

Lin, H.L., Lai, C.T., Ting, H.C., Wang, L.J., Sarnthein, M. and Hung, J.J., 1999. Late Pleistocene nutrients and sea surface productivity in the south China Sea: a record of teleconnections with northern hemisphere events. Marine Geology, 156(1-4): 197-210.

Lin, H.L., Wang, W.C. and Hung, G.W., 2004. Seasonal variation of planktonic foraminiferal isotopic composition from sediment traps in the South China Sea. Marine Micropaleontology, 53(3-4): 447-460.

Lisiecki, L.E. and Raymo, M.E., 2005. A Pliocene-Pleistocene stack of 57 globally distributed benthic delta O-18 records (vol 20, art no PA1003, 2005). Paleoceanography, 20(2).

Liu, K.K., Chao, S.Y., Shaw, P.T., Gong, G.C., Chen, C.C. and Tang, T.Y., 2002. Monsoon-forced chlorophyll distribution and primary production in the South China Sea: observations and a numerical study. Deep-Sea Research Part I-Oceanographic Research Papers, 49(8): 1387-1412.

Liu, Q., Yang, H. and Wang, Q., 2000. Dynamic characteristics of seasonal thermocline in the deep sea region of the South China Sea. Chinese Journal of Oceanology and Limnology, 18(2): 104-109.

Liu, Z., Zhao, Y., Li, J. and Colin, C., 2007. Late Quaternary clay minerals off Middle Vietnam in the western South China Sea: Implications for source analysis and East Asian monsoon evolution. Science in China Series D: Earth Sciences, 50(11): 1674-1684.

Ma, W.T., Chai, F., Xiu, P., Xue, H.J. and Tian, J., 2014. Simulation of export production and biological pump structure in the South China Sea. Geo-Marine Letters, 34(6): 541-554.

Martínez-Botí, M.A., Marino, G., Foster, G.L., Ziveri, P., Henehan, M.J., Rae, J.W.B., Mortyn, P.G. and Vance, D., 2015. Boron isotope evidence for oceanic carbon dioxide leakage during the last deglaciation. Nature, 518(7538): 219-U154.

Ni, Y.Y., Foster, G.L., Bailey, T., Elliott, T., Schmidt, D.N., Pearson, P., Haley, B. and Coath, C., 2007. A core top assessment of proxies for the ocean carbonate system in surface-dwelling foraminifers. Paleoceanography, 22(3).

Noireaux, J., Mavromatis, V., Gaillardet, J., Schott, J., Montouillout, V., Louvat, P., Rollion-Bard, C. and Neuville, D.R., 2015. Crystallographic control on the boron isotope paleo-pH proxy. Earth and Planetary Science Letters, 430: 398-407.

Nurnberg, D., Bijma, J. and Hemleben, C., 1996. Assessing the reliability of magnesium in foraminiferal calcite as a proxy for water mass temperatures (vol 60, pg 803, 1995). Geochimica Et Cosmochimica Acta, 60(13): 2483-2483.

Okazaki, Y., Timmermann, A., Menviel, L., Harada, N., Abe-Ouchi, A., Chikamoto, M.O., Mouchet, A. and Asahi, H., 2010. Deepwater Formation in the North Pacific During the Last Glacial Termination. Science, 329(5988): 200-204.

Oppo, D.W., Linsley, B.K., Rosenthal, Y., Dannenmann, S. and Beaufort, L., 2003. Orbital and suborbital climate variability in the Sulu Sea, western tropical Pacific. Geochemistry Geophysics Geosystems, 4.

Oppo, D.W. and Sun, Y.B., 2005. Amplitude and timing of sea-surface temperature change in the northern South China Sea: Dynamic link to the East Asian monsoon. Geology, 33(10): 785-788.

Ostlund, H.G., 1987. GEOSECS Atlantic, Pacific, and Indiean Ocean Expeditions Vol 7.

Pagani, M., Lemarchand, D., Spivack, A. and Gaillardet, J., 2005. A critical evaluation of the boron isotope-pH proxy: The accuracy of ancient ocean pH estimates. Geochimica Et Cosmochimica Acta, 69(4): 953-961.

Palmer, M.R. and Pearson, P.N., 2003. A 23,000-year record of surface water pH and PCO2 in the western equatorial Pacific Ocean. Science, 300(5618): 480-482.

Rosenthal, Y., Field, M.P. and Sherrell, R.M., 1999. Precise determination of element/calcium ratios in calcareous samples using sector field inductively coupled plasma mass spectrometry. Analytical Chemistry, 71(15): 3248-3253.

Rosenthal, Y. and Linsley, B., 2006. Mg/Ca and Sr/Ca paleothermometery from calcareous marine fossils. Encyclopedia of Quaternary Sciences. Elsevier.

Rosenthal, Y. and Lohmann, G.P., 2002. Accurate estimation of sea surface temperatures using dissolution-corrected calibrations for Mg/Ca paleothermometry. Paleoceanography, 17(3).

Rosenthal, Y., Lohmann, G.P., Lohmann, K.C. and Sherrell, R.M., 2000. Incorporation and preservation of Mg in Globigerinoides sacculifer: Implications for reconstructing the temperature and O-18/O-16 of seawater. Paleoceanography, 15(1): 135-145.

Rosenthal, Y., Oppo, D.W. and Linsley, B.K., 2003. The amplitude and phasing of climate change during the last deglaciation in the Sulu Sea, western equatorial Pacific. Geophysical Research Letters, 30(8).

Rosenthal, Y., Perron-Cashman, S., Lear, C.H., Bard, E., Barker, S., Billups, K., Bryan, M., Delaney, M.L., deMenocal, P.B., Dwyer, G.S., Elderfield, H., German, C.R., Greaves, M., Lea, D.W., Marchitto, T.M., Pak, D.K., Paradis, G.L., Russell, A.D., Schneider, R.R., Scheiderich, K., Stott, L., Tachikawa, K., Tappa, E., Thunell, R., Wara, M., Weldeab, S. and Wilson, P.A., 2004. Interlaboratory comparison study of Mg/Ca and Sr/Ca measurements in planktonic foraminifera for paleoceanographic research. Geochemistry Geophysics Geosystems, 5.

Russell, A.D., Honisch, B., Spero, H.J. and Lea, D.W., 2004. Effects of seawater carbonate ion concentration and temperature on shell U, Mg, and Sr in cultured planktonic foraminifera. Geochimica Et Cosmochimica Acta, 68(21): 4347-4361.

Sanyal, A., Bijma, J., Spero, H. and Lea, D.W., 2001. Empirical relationship between pH and the boron isotopic composition of Globigerinoides sacculifer: Implications for the boron isotope paleo-pH proxy. Paleoceanography, 16(5): 515-519.

Sarmiento, J.L., 2013. Ocean biogeochemical dynamics. Princeton University Press.

Schiebel, R. and Hemleben, C., 2017. Planktic Foraminifers in the Modern Ocean. Springer-Verlag Berlin Heidelberg.

Schmitt, J., Schneider, R., Elsig, J., Leuenberger, D., Lourantou, A., Chappellaz, J., Kohler, P., Joos, F., Stocker, T.F., Leuenberger, M. and Fischer, H., 2012. Carbon Isotope Constraints on the Deglacial CO2 Rise from Ice Cores. Science, 336(6082): 711-714.

Simon, L., Lecuyer, C., Marechal, C. and Coltice, N., 2006. Modelling the geochemical cycle of boron: Implications for the long-term delta B-11 evolution of seawater and oceanic crust. Chemical Geology, 225(1-2): 61-76.

Spero, H.J., Eggins, S.M., Russell, A.D., Vetter, L., Kilburn, M.R. and Honisch, B., 2015. Timing and mechanism for intratest Mg/Ca variability in a living planktic foraminifer. Earth and Planetary Science Letters, 409: 32-42.

Spezzaferri, S., Kucera, M., Pearson, P.N., Wade, B.S., Rappo, S., Poole, C.R., Morard, R. and Stalder, C., 2015. Fossil and Genetic Evidence for the Polyphyletic Nature of the Planktonic Foraminifera "Globigerinoides", and Description of the New Genus Trilobatus. Plos One, 10(5).

Steinke, S., Glatz, C., Mohtadi, M., Groeneveld, J., Li, Q.Y. and Jian, Z.M., 2011. Past dynamics of the East Asian monsoon: No inverse behaviour between the summer and winter monsoon during the Holocene. Global and Planetary Change, 78(3-4): 170-177.

Steinke, S., Mohtadi, M., Groeneveld, J., Lin, L.C., Lowemark, L., Chen, M.T. and Rendle-Buhring, R., 2010. Reconstructing the southern South China Sea upper water column structure since the Last Glacial Maximum: Implications for the East Asian winter monsoon development. Paleoceanography, 25.

Su, C.M. and Suarez, D.L., 1995. Coordination of Adsorbed Boron - a Ftir Spectroscopic Study. Environmental Science & Technology, 29(2): 302-311.

Su, X., Liu, C.L., Beaufort, L., Tian, J. and Huang, E.Q., 2013. Late Quaternary coccolith records in the South China Sea and East Asian monsoon dynamics. Global and Planetary Change, 111: 88-96.

Takahashi, T., Sutherland, S.C., Wanninkhof, R., Sweeney, C., Feely, R.A., Chipman, D.W., Hales, B., Friederich, G., Chavez, F., Sabine, C., Watson, A., Bakker, D.C.E., Schuster, U., Metzl, N., Yoshikawa-Inoue, H., Ishii, M., Midorikawa, T., Nojiri, Y., Kortzinger, A., Steinhoff, T., Hoppema, M., Olafsson, J., Arnarson, T.S., Tilbrook, B., Johannessen, T., Olsen, A., Bellerby, R., Wong, C.S., Delille, B., Bates, N.R. and de Baar, H.J.W., 2009. Climatological mean and decadal change in surface ocean pCO(2), and net sea-air CO2 flux over the global oceans. Deep-Sea Research Part Ii-Topical Studies in Oceanography, 56(8-10): 554-577.

Tian, J., Huang, E.Q. and Pak, D.K., 2010. East Asian winter monsoon variability over the last glacial cycle: Insights from a latitudinal sea-surface temperature gradient across the South China Sea. Palaeogeography Palaeoclimatology Palaeoecology, 292(1-2): 319-324.

Tian, J., Pak, D.K., Wang, P.X., Lea, D., Cheng, X.R. and Zhao, Q.H., 2006. Late Pliocene monsoon linkage in the tropical South China Sea. Earth and Planetary Science Letters, 252(1-2): 72-81.

Tseng, C.M., Wong, G.T.F., Chou, W.C., Lee, B.S., Sheu, D.D. and Liu, K.K., 2007. Temporal variations in the carbonate system in the upper layer at the SEATS station. Deep-Sea Research Part Ii-Topical Studies in Oceanography, 54(14-15): 1448-1468.

Wan, S. and Jian, Z.M., 2014. Deep water exchanges between the South China Sea and the Pacific since the last glacial period. Paleoceanography, 29(12): 1162-1178.

Wang, B.S., You, C.F., Huang, K.F., Wu, S.F., Aggarwal, S.K., Chung, C.H. and Lin, P.Y., 2010. Direct separation of boron from Na- and Ca-rich matrices by sublimation for stable isotope measurement by MC-ICP-MS. Talanta, 82(4): 1378-1384.

Wang, D., Du, Y. and Shi, P., 2002. Climatological atlas of physical oceanography in the upper layer of the South China Sea. Meteorol. Press, Beijing, 168pp (in Chinese).

Wang, L., Sarnthein, M., Erlenkeuser, H., Grimalt, J.O., Grootes, P., Heilig, S., Ivanova, E., Kienast, M., Pelejero, C. and Pflaumann, U., 1999. East Asian monsoon climate during the Late Pleistocene: high-resolution sediment records from the south China Sea. Marine Geology, 156(1-4): 245-284.

Wang, P. and Li, Q., 2009. The South China Sea. Developments in Paleoenvironmental Research, 13. Springer Netherlands, X, 506 pp.

Wang, P.X., Li, Q.Y., Tian, J., He, J., Jian, Z.M., Ma, W.T. and Dang, H.W., 2016. Monsoon influence on planktic delta O-18 records from the South China Sea. Quaternary Science Reviews, 142: 26-39.

Wang, X. and Li, B., 2012. Sea surface temperature evolution in the western South China Sea since MIS 12 as evidenced by planktonic foraminiferal assemblages and Globigerinoides ruber Mg/Ca ratio. Science China Earth Sciences, 55(11): 1827-1836.

Wang, Y.J., Cheng, H., Edwards, R.L., An, Z.S., Wu, J.Y., Shen, C.C. and Dorale, J.A., 2001. A high-resolution absolute-dated Late Pleistocene monsoon record from Hulu Cave, China. Science, 294(5550): 2345-2348.

Wei, G.J., Deng, W.F., Liu, Y. and Li, X.H., 2007. High-resolution sea surface temperature records derived from foraminiferal Mg/Ca ratios during the last 260 ka in the northern South China Sea. Palaeogeography Palaeoclimatology Palaeoecology, 250(1-4): 126-138.

Weldeab, S., Lea, D.W., Schneider, R.R. and Andersen, N., 2007. 155,000 years of West African monsoon and ocean thermal evolution. Science, 316(5829): 1303-1307.

Wu, Q., Colin, C., Liu, Z.F., Thil, F., Dubois-Dauphin, Q., Frank, N., Tachikawa, K., Bordier, L. and Douville, E., 2015. Neodymium isotopic composition in foraminifera and authigenic phases of the South China Sea sediments: Implications for the hydrology of the North Pacific Ocean over the past 25 kyr. Geochemistry Geophysics Geosystems, 16(11): 3883-3904.

Wyrtki, K., 1961. Physical oceanography of the Southeast Asian waters. Scripps Institution of Oceanography.

Xie, S.P., Xie, Q., Wang, D.X. and Liu, W.T., 2003. Summer upwelling in the South China Sea and its role in regional climate variations. Journal of Geophysical Research-Oceans, 108(C8).

Yu, J.M., Elderfield, H., Greaves, M. and Day, J., 2007. Preferential dissolution of benthic foraminiferal calcite during laboratory reductive cleaning. Geochemistry Geophysics Geosystems, 8.

Yu, P.-S., Mii, H.-S., Murayama, M. and Chen, M.-T., 2008. Late Quaternary Planktic Foraminifer Fauna and Monsoon Upwelling Records from the Western South China Sea, Near the Vietnam Margin (IMAGES MD012394). Terrestrial, Atmospheric & Oceanic Sciences, 19(4).

Yu, P.S., Huang, C.C., Chin, Y., Mii, H.S. and Chen, M.T., 2006. Late Quaternary East Asian Monsoon variability in the South China Sea: Evidence from planktonic foraminifera

faunal and hydrographic gradient records. Palaeogeography Palaeoclimatology Palaeoecology, 236(1-2): 74-90.

Zeebe, R.E., Bijma, J. and Wolf-Gladrow, D.A., 1999. A diffusion-reaction model of carbon isotope fractionation in foraminifera. Marine Chemistry, 64(3): 199-227.

Zeebe, R.E. and Wolf-Gladrow, D.A., 2001. CO2 in seawater: equilibrium, kinetics, isotopes. Gulf Professional Publishing.

Zhai, W.D., Dai, M.H., Chen, B.S., Guo, X.H., Li, Q., Shang, S.L., Zhang, C.Y., Cai, W.J. and Wang, D.X., 2013. Seasonal variations of sea-air CO2 fluxes in the largest tropical marginal sea (South China Sea) based on multiple-year underway measurements. Biogeosciences, 10(11): 7775-7791.

Zhang, H.B., Griffiths, M.L., Huang, J.H., Cai, Y.J., Wang, C.F., Zhang, F., Cheng, H., Ning, Y.F., Hu, C.Y. and Xie, S.C., 2016. Antarctic link with East Asian summer monsoon variability during the Heinrich Stadial-Bolling interstadial transition. Earth and Planetary Science Letters, 453: 243-251.
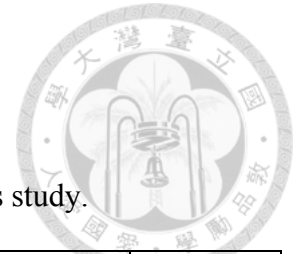
Appendix

Table S1. Chemical data for *G. sacculifer* (w/o sac) from W-SCS in this study.

Sample	ID	Age (kyr)	Mg/Ca (mmol/mol)	SST (℃)	Ba/Ca (μmol/mol)	Mn/Ca (μmol/mol)	Fe/Ca (μmol/mol)	Al/Ca (μmol/mol)
A1	1	0.02	3.57	26.9	6.2	638.1	9.1	7.5
A2	13	2.12	3.80	27.6	4.0	686.4	14.5	4.1
A3	19	3.8	3.89	27.9	1.4	460.4	14.3	2.8
A4	22	6.6	3.79	27.6	1.5	493.7	11.2	6.1
A5	25	9.3	3.66	27.2	1.5	585.7	18.9	3.9
A6	27	11.1	3.37	26.3	1.6	588.1	18.4	3.8
A7	28	12	3.36	26.3	1.7	565.0	19.8	3.0
A8	29	12.75	3.14	25.6	2.0	380.7	15.9	3.1
A9	31	14.25	3.22	25.8	2.3	404.5	20.0	2.4
A10	32	15	3.13	25.5	4.0	440.7	24.5	2.7
A11	33	15.75	2.92	24.7	1.2	366.8	21.2	2.5
A12	34	16.5	2.99	25.0	1.1	420.2	23.9	3.9
A13	35	17.25	2.972	24.9	1.2	436.4	23.8	4.3
A14	37	18	3.12	25.5	1.5	637.7	34.2	3.7
A15	41	22.04	2.72	23.9	1.5	601.1	26.4	3.4

Table S2. The $\delta^{11}B$, calculated pH_{SW}, $pH_{equilibrium}$ and $\Delta pH_{(sea\text{-}air)}$ of *G. sacculifer* (w/o sac) from W-SCS in this study.

Sample	ID	Age (kyr)	$\delta^{11}B$ (‰)	2SD (‰)	pH_{SW}	$pH_{equilibrium}$	$\Delta pH_{(sea\text{-}air)}$
A1	1	0.02	19.72	0.22	8.16	8.18	-0.02
A2	13	2.12	20.06	0.22	8.20	8.19	0.01
A3	19	3.8	19.09	0.26	8.10	8.19	-0.09
A4	22	6.6	19.08	0.34	8.10	8.20	-0.10
A5	25	9.3	18.97	0.27	8.09	8.19	-0.10
A6	27	11.1	18.78	0.24	8.07	8.19	-0.12
A7	28	12	18.58	0.40	8.05	8.22	-0.17
A8	29	12.75	19.88	0.20	8.18	8.23	-0.05
A9	31	14.25	19.58	0.20	8.15	8.23	-0.08
A10	32	15	20.07	0.22	8.20	8.25	-0.05
A11	33	15.75	19.68	0.21	8.16	8.25	-0.09
A12	34	16.5	19.43	0.26	8.14	8.28	-0.14
A13	35	17.25	19.90	0.43	8.18	8.30	-0.12
A14	37	18	19.07	0.33	8.10	8.31	-0.21
A15	41	22.04	18.79	0.31	8.14	8.31	-0.17